NUMERICAL AND EXPERIMENTAL INVESTIGATION OF SHELL-AND-TUBE PHASE CHANGE MATERIAL THERMAL STORAGE UNIT

A Thesis
Presented to
The Academic Faculty

by

Thomas H Sherer II

In Partial Fulfillment
Of the Requirements for the Degree
Master of Science in Mechanical Engineering

Georgia Institute of Technology
May 2015

NUMERICAL AND EXPERIMENTAL INVESTIGATION OF SHELL-AND-TUBE PHASE CHANGE MATERIAL THERMAL STORAGE UNIT

Approved by:

Dr. Yogendra Joshi, Advisor
School of Mechanical Engineering
Georgia Institute of Technology

Dr. Sushil Bhavnani
School of Mechanical Engineering
Auburn University

Dr. Samuel Graham
School of Mechanical Engineering
Georgia Institute of Technology

Dr. Madhusudan Iyengar
Google Inc.

Date Approved: April 21, 2015

ACKNOWLEDGMENTS

To my Lord and Savior, Jesus Christ, thank You for loving me so immeasurably that You died in my place on the cross, taking upon Yourself the full wrath of God for my sins. It is my desire to live for You, the Savior of my soul.

Dad and Mom, I cannot express how thankful I am to God for blessing me with such loving, caring, prayerful parents. Thank you for energizing me throughout this research with your continual encouragement via letters, notes, phone calls, and texts. Tyler and Amanda, it is a tremendous privilege and pleasure to be your brother, and your prayers and kindness have ministered to me in ways you will never know.

Dr. Joshi, thank you for the opportunity to perform research for and with you. You have been a blessing in my life, and I have greatly enjoyed learning from you. Dr. Bhavnani, thank you for giving me my first research opportunity at Auburn University. Dr. Iyengar, thank you for your valuable input and advice throughout the project. Dr. Graham, thank you for taking the time to be an important part of my thesis committee.

Thank you, Brandon Royal, for helping me with the experimental fabrication, and for your patience with my many questions. Thank you, Dr. Garimella and Chris Keinath, for allowing us to use the environmental chamber for PCM melting. To my colleagues in the Microelectronics & Emerging Technologies Thermal Laboratory, thank you for your friendship. Thank you, Google, for funding this work through a Google Research Award.

Finally, and very importantly, thank you to everyone in Anniston Bible Church and Grace Atlanta Bible Church who has prayed for and encouraged me during this work. You are indescribably special to me, and I am eternally thankful to God for you.

TABLE OF CONTENTS

LIST OF TABLES

LIST OF FIGURES

NOMENCLATURE

C_k	specific heat of phase k in PCM [J/kg-K]
C_{HTF}	specific heat of heat transfer fluid [J/kg-K]
E	internal energy [J]
f	liquid fraction of melt
g	gravitational acceleration [m/s^2]
h	sensible volumetric enthalpy [J/m^3]
h_{in}	sensible enthalpy of HTF entering control volume [J/kg]
H	total volumetric enthalpy [J/m^3]
HTC	heat transfer coefficient [W/m^2-K]
k	thermal conductivity [W/m-K]
L	latent heat of fusion [J/kg]
k_f	k factor for student's t distribution
m	mass [kg]
$\dot{m}$	mass flow rate [kg/s]
N	number of tubes in a column of the tube bank
n	number of temperature samples for calibration and uncertainty
r	radius [m]
Ra	Rayleigh number, $g\beta(T_w - T_m)R_w^3/(\nu\alpha_l)$
R_w	radius of cylinder wall for Ra calculation [m]

S_L	longitudinal pitch of tube bank [m]
S_T	transverse pitch of tube bank [m]
S_x	standard deviation of temperature [°C]
Sc	subcooling number, $C_s(T_m - T_o)/L$
Ste	Stefan number, $C_l(T_w - T_m)/L$
t	time [s]
T	temperature [K]
$T_{HTF,in}$	temperature of inlet HTF [K]
$T_{HTF,out}$	temperature of outlet HTF [K]
T_m	melting/freezing temperature of PCM [K]
T_o	initial temperature [K]
T_w	wall temperature [K]
Δt	time step [s]
TOL	tolerance factor
U_A	Type A uncertainty in temperature [°C]
U_B	Type B uncertainty in temperature [°C]
U_{Cal}	calibration uncertainty in dry block calibrator [°C]
U_{Res}	resolution uncertainty in dry block calibrator [°C]
$\bar{x}$	sample mean temperature [°C]
x_i	sample temperature [°C]

Greek Symbols

α	thermal diffusivity [m^2/s]
β	thermal expansion coefficient [K^{-1}]
μ	true population mean of temperature [°C]
ν	kinematic viscosity [m^2/s]
ρ	density [kg/m^3]

Subscripts

ct	cylindrical tube value
HTF	heat transfer fluid
l	liquid value
n	specified bulk water control volume
s	solid value
W, P, E	west, center, east nodal locations
w, e	west and east interface locations

Superscripts

o	old time step value
k	iteration level

SUMMARY

Latent heat thermal energy storage (TES) is becoming an increasingly popular approach for effective energy conservation. Significant amounts of energy can be stored in relatively small volumes of material by taking advantage of the high latent heat of solid-liquid phase change materials (PCMs). Storing large amounts of energy in this space-effective manner is very attractive for data center applications where considerable resources are expended to cool electronics. By utilizing the energy storage capabilities of a TES unit in a data center during on- and off-peak hours, energy costs can be significantly diminished.

This thesis addresses the numerical and experimental investigation of a TES unit with water acting as the heat transfer fluid (HTF) in crossflow over a bank of PCM-filled tubes. The numerical simulations employ a fully-implicit transient one-dimensional control volume formulation that utilizes the enthalpy method for phase change. The phase change process for the tube bank is coupled with the conservation of energy to determine the bulk HTF temperature exiting each column of tubes and ultimately the tube bank. Experimentation, using commercial paraffin RUBITHERM RT 28 HC PCM, has been performed for model validation, and the transient numerical simulation results are compared with the experimental findings.

CHAPTER 1

INTRODUCTION AND BACKGROUND

The rise in energy consumption by data centers over the last few decades has necessitated technological progress in nearly every field of engineering. The electricity usage of data centers as a percentage of the total electricity usage in the United States has increased from around 0.12% in 2000 [1] to between 1.7 and 2.2% in 2010 [2]. The increased performance of computing equipment in a cost-effective way has demanded electrical, mechanical, material, and chemical innovations. Energy efficiency of the equipment is a relatively new concern.

One of the primary contributors to the high power consumption in data centers is the cooling hardware, often comprising 30-50% of a data center's energy consumption [3]. It is imperative to develop techniques to meet this cooling requirement in a cost-effective manner. Traditionally, this equipment is cooled by drawing air directly through the servers. In most air-cooled high performance data centers, Computer Room Air Conditioning (CRAC) units supply chilled air to the server room through floor perforated tiles on a raised floor plenum [4]. The racks are arranged such that the server fans draw chilled air into the front and expel hot air out the back, effectively creating hot and cold aisles between rack rows. After exiting the servers the hot air is returned to the CRAC units to be chilled by refrigerated water in a chiller/cooling tower loop [5]. Figure 1.1 illustrates this process. While this air cooling method is simple, because it is limited in its

cooling capacity and cost-effectiveness, many companies are pursuing more cost-effective alternatives to supply increased cooling to increasing electronic power loads.

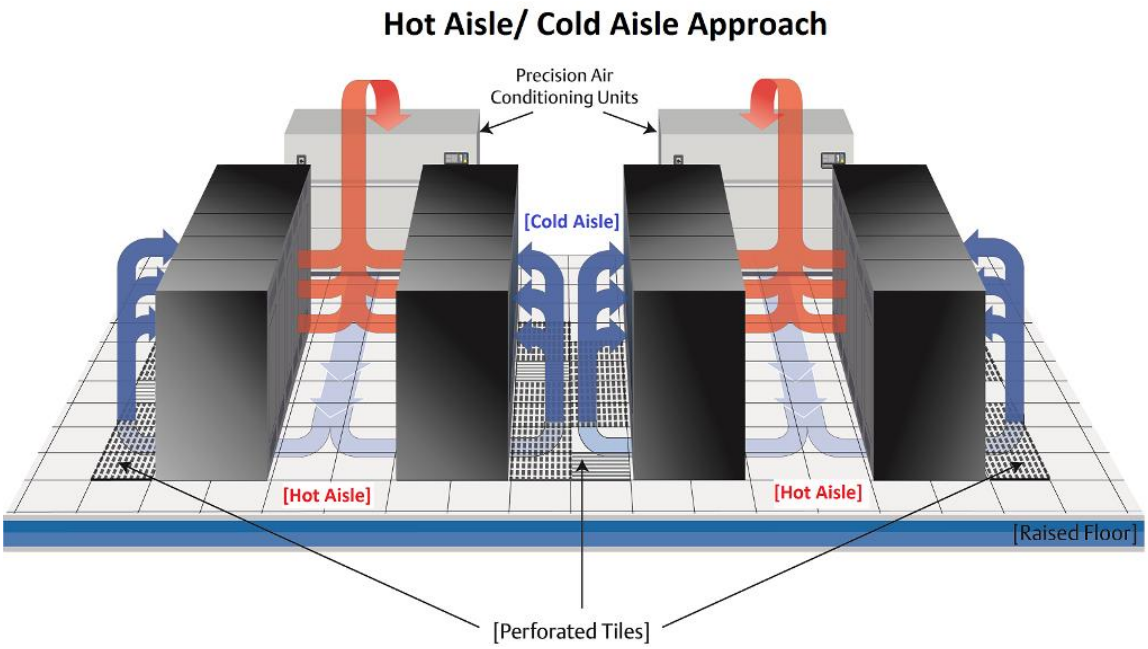

Figure 1.1: Air-Cooled Data Center with Hot Aisle / Cold Aisle Approach [6]

One such alternative, direct liquid cooling, has been shown by Greenberg et al. [7] to be noticeably more economical than air cooling. A schematic of a direct liquid cooling system by Asetek is shown in Figure 1.2. In this Asetek cooling system cold water is directly used to absorb heat from the central processing unit (CPU) via a cold plate, and from the memory dual in-line memory modules (DIMMs) via a manifold. After the water has absorbed heat from the CPU and DIMMs, it returns to the Asetek RackCDU^{TM} to exchange heat with another liquid which is circulated out from the RackCDU^{TM} and utilized for waste heat recycling. In this application not every electronic component in the server is cooled via direct liquid cooling, requiring some amount of air cooling, but

because most of the heat is dissipated using liquid cooling, air cooling energy usage is reduced [8].

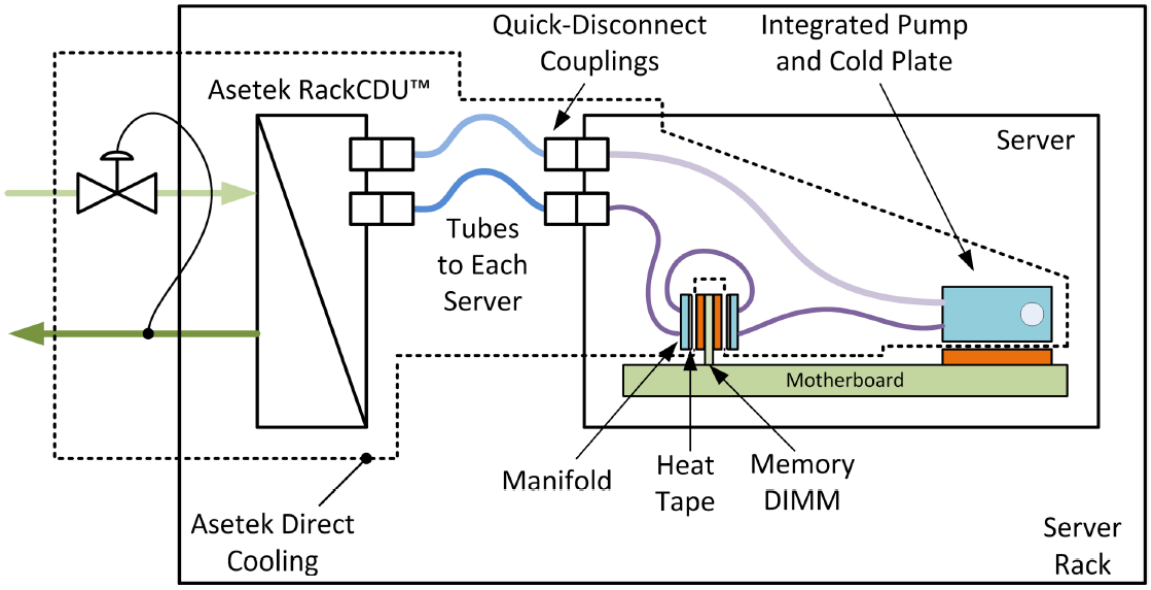

Figure 1.2: Schematic: Direct Cooling System [8]

While the Asetek system employs waste heat recycling, most direct liquid cooling applications simply use an internal coolant loop to absorb the heat from the processors and memory modules via cold plates, and then exchange that heat with an external coolant loop, which ultimately dispels the heat to the ambient air [5]. This form of direct liquid cooling has not been fully embraced due to concerns of short-circuits from leakage [9]. Another form of direct liquid cooling is liquid immersion of the electronics into an oil or dielectric material. Though this approach provides excellent heat transfer through boiling, its implementation has been hindered by the inaccessibility of the equipment [9].

Because cold water is often used in some capacity, whether directly or indirectly, to cool servers within a data center, it is desirable to formulate a cost-effective way to chill

the water. Electrical costs necessary to chill water with typical refrigeration cycles are undesirably high during peak hours of electrical usage when electricity is more expensive. Therefore, rather than using a costly refrigeration cycle to chill the water during peak hours, it would be economically beneficial to employ a system whereby the refrigeration cycle is operated during off-peak hours to store cold energy for use during peak hours.

Such thermal energy storage occurs in two primary forms: sensible heat storage and latent heat storage. Cold energy in the form of sensible heat can be stored by simply lowering the temperature of a material in a single phase. To store a significant quantity of energy in this way requires a large volume of material, and the release of this energy will likely take place over a large temperature range. By storing cold energy in the form of latent heat, however, a nearly isothermal transfer of heat with a considerably smaller mass of material is possible. For example, between 5°C - 15°C water can store 41.94 kJ/kg of sensible heat; whereas between -5°C - 5°C water/ice can store 365.21 kJ/kg of sensible and latent heat, demonstrating that by exploiting water's latent heat, less water is needed to store a specified amount of energy. The amount of storable energy between the solid and liquid phases of a material is determined by the material's density and latent heat of fusion; materials that have high values for these two properties are capable of storing a significant amount of energy in a small volume. While every material stores some amount of latent heat during transition between solid and liquid phases, some materials are specifically utilized for their superior capacity to store latent heat, and these are commonly known as phase change materials (PCMs). Using these PCMs to store large quantities of energy in a space-effective manner is very attractive for data centers

seeking to chill water in a cost-effective way by storing cold energy during off-peak hours.

1.1 Phase Change Materials

PCMs are often classified by their material composition, and while in-depth classification of these materials can be found in the literature [10], a simple, straightforward classification has been presented by Sharma et al. [11] and is provided in Figure 1.3. The three primary PCM subgroups are organics (paraffins and non-paraffins), inorganics (salt hydrates and metallics), and eutectics. Each subgroup of PCM has its own set of advantages and disadvantages to consider when choosing a PCM for an application, and some of the most desirable characteristics (for most applications) include the following: a suitable melting/freezing temperature, high latent heat of fusion, high density, high specific heat, high thermal conductivity, low volumetric expansion, cyclical stability, cost-effectiveness, and safety (non-flammable, non-poisonous, non-corrosive) [11]. The two most commercially dominant subgroups of PCM are paraffins compounds and salt hydrates [10].

1.1.1 Paraffins

Likely the most commonly used subgroup of organic PCMs is paraffin compounds. Technical grade paraffins, which are saturated hydrocarbons, are widely available at low cost (~$130/kWh) and a wide range of melting temperatures with a relatively high latent heat of fusion (140-250 kJ/kg), making them viable candidates for various thermal applications [12]. They also exhibit good cyclical stability and thermal reliability through

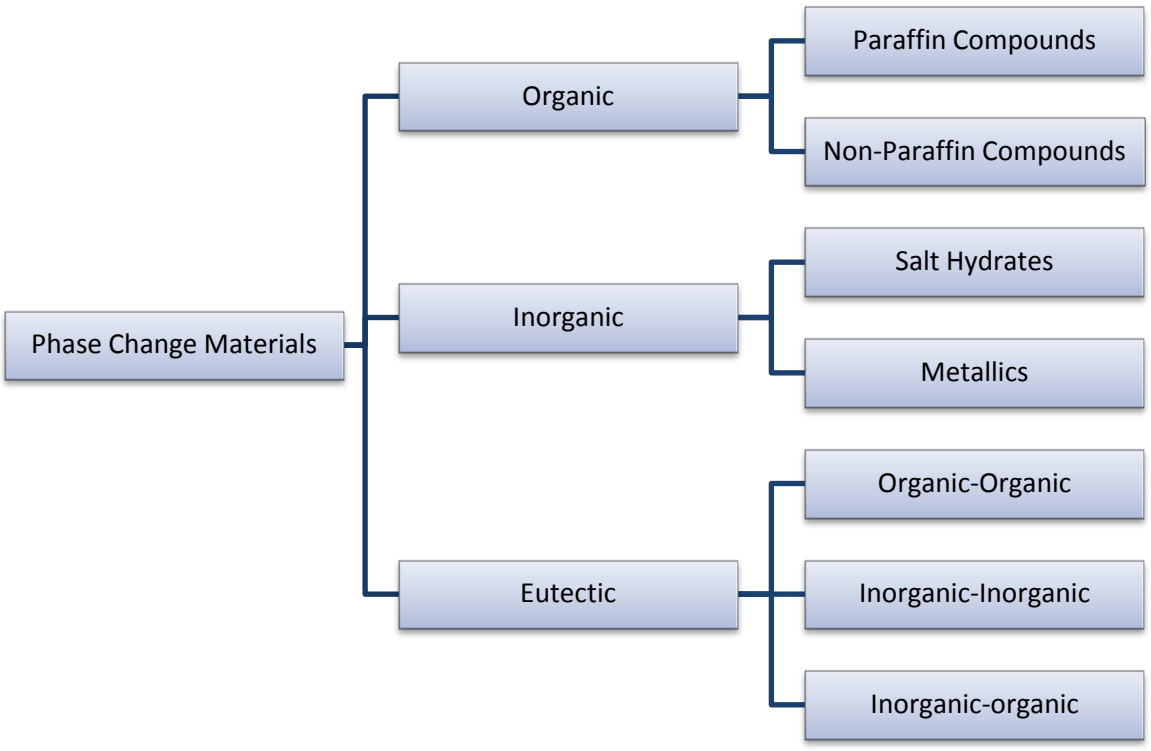

Figure 1.3: Classification of Phase Change Materials [11]

their lifetime, and are considered non-toxic [10]. The moderately low density of paraffins (700-900 kg/m^3) necessitates a larger volume of PCM to store energy, an undesirable shortcoming in many applications. The most significant drawback, however, to paraffins is their low thermal conductivity (~0.2 W/m-K) which inhibits timely heat transfer. This issue is particularly concerning in thermal storage units, where low thermal conductivity leads to undesirably longer charging and discharging times within a TES unit. This issue can be mitigated to promote faster charging and discharging by either adding a material to the PCM with a higher thermal conductivity, by using fins to promote heat transfer, or by packaging the PCM within the storage unit in small containers or capsules for a higher PCM surface area to volume ratio.

1.1.2 Salt Hydrates

Salt hydrates, the chief subgroup within inorganic PCMs, are mixtures of inorganic salts and water. Having both high latent heat of fusion (150-300 kJ/kg) and high density (1000-1900 kg/m^3), salt hydrates are capable of storing large quantities of energy in small volumes. Relative to paraffins, they have higher thermal conductivity (0.4-0.7 W/m-K), which promotes faster melting and freezing times, and tend to be slightly more expensive (~$140/kWh), with some exceptions [12]. The major disadvantages for salt hydrates involve subcooling, phase segregation, and corrosiveness [13]. When a salt hydrate exhibits subcooling, it solidifies by crystallization below the melting temperature. This is problematic in many applications because a well-established, consistent freezing temperature is necessary, and significant subcooling could prevent latent heat storage. Nucleating agents can often be introduced to the PCM to provide sites for nucleation, preventing significant subcooling. Salt hydrates also face the issue of phase segregation which limits their effectiveness in certain applications because it leads to incongruent melting and sedimentation. This issue can be mitigated with the addition of a thickening agent. Concerning the issue of corrosiveness, salt hydrates have proven to be damaging to certain containment materials, so it is necessary to understand their compatibility with other materials prior to their application [14].

1.1.3 Applications

Over the last half century, PCMs have played an increasingly important role in providing effective solutions to numerous thermal management challenges. Several images of PCM applications are provided in Figure 1.4. Beginning in the 1960s, NASA

investigated and utilized paraffin wax for spacecraft thermal control. By applying PCMs to certain electronics on the Lunar Roving Vehicle in the 1971 Apollo 15 mission, they effectively protected the Signal Processing Unit and batteries, the Drive Control Electronics, and the Lunar Communications Relay Unit by absorbing heat during use and then radiating that heat into space afterward [15].

In the 1980s NASA introduced microencapsulated PCMs into space suits to provide thermal stability for the astronauts in extreme thermal environments [16]. Commercial textile companies have hence adapted similar technologies for use in a variety of applications. Outlast Technologies Inc. has incorporated PCMs into fabrics for use in a variety of products including bedding products, shirts, gloves, shoes, and car seats. With a flame retardant T-shirt designed specifically for military application, an Outlast® shirt outperformed similar shirts of modacrylic fiber by reducing sweat by as much as 34% [17].

The nearly constant temperature maintained by PCMs during phase change is very advantageous for applications in shipping temperature-sensitive items. Certain food products, high-tech electronic devices, and pharmaceuticals require thermal protection during distribution. The shipment of blood, organs, and tissues also demands very strict temperature requirements. These needs can be met by strategically placing PCM-filled containers within the shipment container to maintain the item's temperature over the course of the shipment. Companies such as PCM Products Ltd, Pelican BioThermal, Cryopak, and RGEES, LLC produce PCMs and containers for these thermal shipment applications.

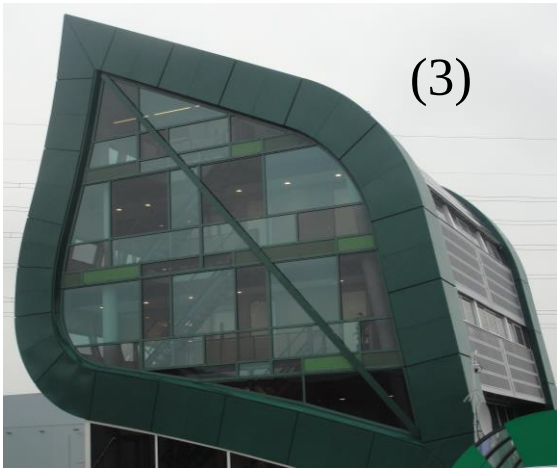

(1) Outlast® spacesuit and bedding with PCM (www.outlast.com)
(2) TechKewl phase change cooling vest (www.safetyandbootcenter.com)
(3) PCM-cooled office building in Netherlands (www.pcmenergy.com)
(4) PCM installed in ceiling (www.climatetechwiki.org)
(5) PCM-cooled shipping container (www.cryopak.com)
(6) Rubitherm PCM pack for transport (www.ruhrtech.com)

Figure 1.4: Phase Change Material Applications

The energy storage capacity of PCMs has also attracted the attention of the solar energy community. Because solar energy is only available during part of the day, it is necessary to store a portion of energy absorbed for nighttime use when solar energy is unavailable. By thermally storing this energy in a PCM, relatively significant quantities of energy can be importantly stored in small volumes, due to the high latent heat of PCM. Among other issues, the low thermal conductivity of PCM and the imperfections of energy storage currently limit the effectiveness of the thermosolar energy system, but researchers continue to pursue advancements in these areas to overcome these issues. A detailed review of solar cooling methods and thermal storage options has been published by Chidambaram et al. [18].

Many applications exist for PCM-based thermal energy storage within buildings, but passive building systems have possibly received the most attention in the last few years. In a PCM-based passive building system, PCM is placed in the building envelopes to act as a heat sink during the day, and a heat source during the night. When implemented in a hot environment, the PCM melts during the day, absorbing the heat that otherwise would have been conducted further into the building structure, thereby mitigating the requirements on the air conditioning unit. At night, when the ambient temperature is lower, the PCM releases its stored energy and re-freezes. This heat loss from the PCM could reduce the nighttime heater load, depending on the ambient temperature. The PCM must be carefully chosen for each individual application to ensure that complete freezing can occur at night, since failure to refreeze results in decreased effectiveness. If appropriately applied, PCM-based passive building systems can reduce

electrical energy costs and improve temperature stability. More information concerning PCM usage in building applications can be found in a paper by Kalnæs and Jelle [19].

1.2 PCM-Based Thermal Energy Storage

PCMs have been employed in numerous applications because of their superior ability to store large quantities of energy in small volumes at a near-constant temperature. While PCMs have been used for thermal control and stability, arguably the primary application of PCMs is thermal energy storage for intentional reuse. PCM-based TES units have been increasingly studied in the past several years, yielding important results regarding PCM usage, containment geometries, and heat transfer modes. A detailed review of PCM materials, latent heat TES systems, heat transfer enhancement techniques, and phase change problem formulation has been published by Agyenim et al. [20].

The most studied TES geometry is the concentric shell-and-tube geometry shown in Figure 1.5. While this geometry is safe and reliable, the low surface area to volume ratio of the PCM results in long charging/discharging times due to the low thermal conductivity of the PCM. Adding longitudinal or circular fins, as shown in Figure 1.6, increases the effective thermal conductivity of the unit. Another strategy used for containment of the PCM within a TES unit is spherical encapsulation within a polymer, as shown in Figure 1.7. This provides a higher surface area to volume ratio of the PCM, mitigating the negative effects of the PCM's low thermal conductivity. If however, one of these spheres is punctured, PCM will flow into the HTF, causing many problems. A unit that combines the reliability and safety of the concentric units with the improved

effective thermal conductivity of the spherically encapsulated PCM unit would enhance thermal energy storage.

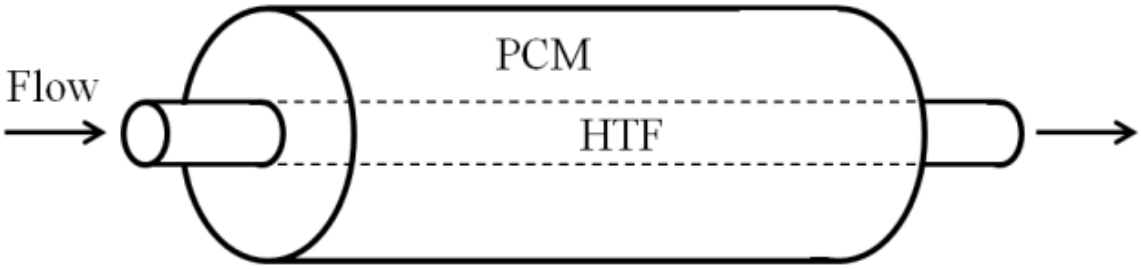

Figure 1.5: Concentric Shell-and-Tube PCM TES Unit

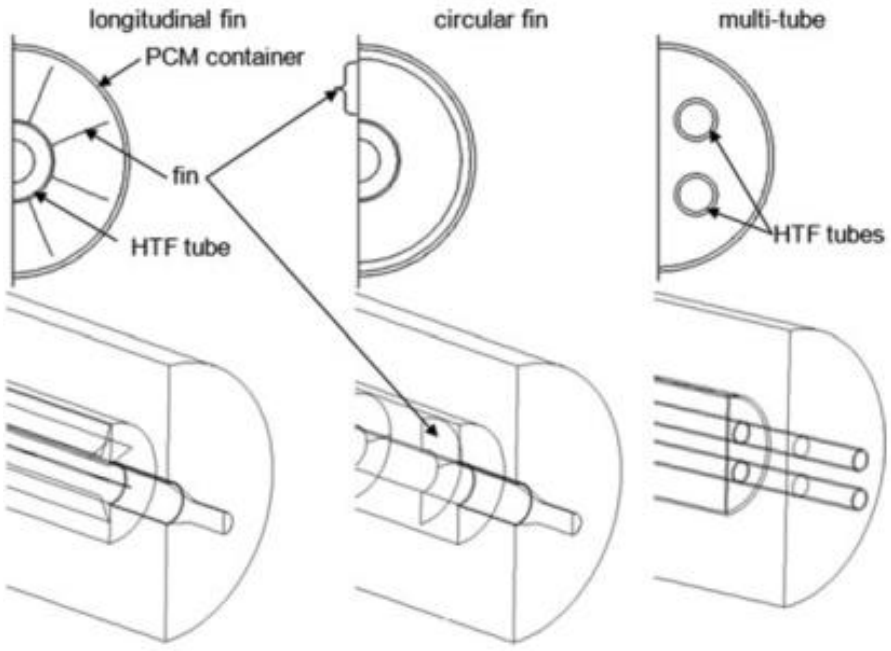

Figure 1.6: Concentric Shell-and-Tube PCM TES Unit Variations [21]

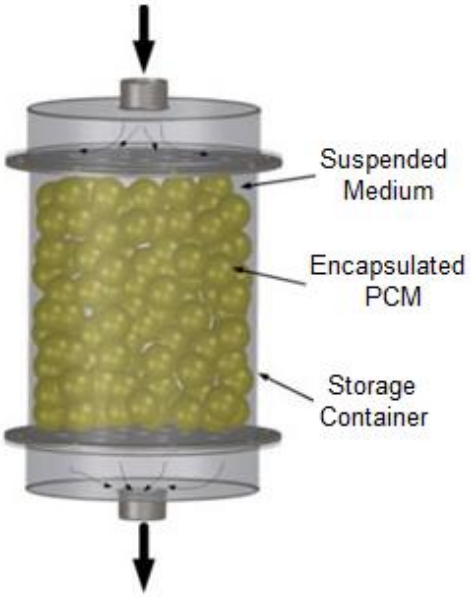

Figure 1.7: TES Unit with PCM-Filled Spheres [22]

Trp [23] and Trp et al. [24] numerically and experimentally analyzed a vertically-oriented cylindrical TES unit with several HTF tubes surrounded by a shell filled with PCM. They suggested that the numerical results obtained in their simulations for various geometries and HTF parameters can be used for design optimization to ensure suitable system performance. Vyshak and Jilani [25] numerically analyzed three individual PCM containers – rectangular, cylindrical, and cylindrical shell – with HTF flowing around, or through in the case of the cylindrical shell, the length of the containers. Using containers having the same volume and surface area of heat transfer, they determined that the cylindrical shell container requires the least amount of time for energy storage. They found further that with more PCM mass added to each configuration this storage time difference became increasingly more pronounced.

Agyenim et al. [26-29] studied both a single tube and a multi-tube concentric unit and found that the multi-tube approach results in considerably faster charging/discharging

times. They also concluded that convective heat transfer is even more dominant in a multi-tube approach than a single tube approach. They further studied the charging and discharging cycles of single tube concentric units with radial and longitudinal fins to assess their effectiveness for energy storage compared to finless units, concluding that longitudinal fins promote faster charging/discharging cycles. Mosaffa et al. [30] also studied concentric units with radial fins for comparison with rectangular storage units.

Ezan et al. [31] experimentally and numerically studied a concentric shell-and-tube PCM unit and determined that convection played a more significant role than conduction after a short conduction-dominated period. This result would be expected for PCM units with large bulk volumes of PCM. While most analyses in the literature involve a bulk volume of PCM within a shell-and-tube TES unit, Dubovsky et al. [32] employed a tube bank within a rectangular unit with PCM in the cylindrical tubes and air acting as the HTF in crossflow. With the assumption that the sensible heat capacity of the PCM and the tubes is small compared to the latent heat of the PCM, the system was solved analytically to compare with a numerical simulation. Increasingly more numerical and experimental work is being done to investigate shell-and-tube PCM units with bulk PCM volumes [21,33-35] but relatively little work has been performed on TES units with a tube bank of PCM-filled tubes in crossflow, a design with potentially significant advantages due to a higher PCM surface area to volume ratio. Parry et al. [21], for example, studied multiple TES concentric unit configurations (single HTF tube, single HTF tube with radial fins, single HTF tube with longitudinal fins, and four HTF tubes) with PCM surface area to volume ratios between 11.67-54.61 m^{-1}. The shell-and-tube PCM TES in the present study has a PCM surface area to volume ratio of 2113.83 m^{-1}.

The focus of this study is to numerically and experimentally investigate a TES unit with water acting as the HTF in crossflow over a bank of PCM-filled tubes. This geometry, shown more fully in the following chapter, is safe and reliable, and has a high PCM surface area to volume ratio. The numerical simulations employ a fully-implicit transient one-dimensional control volume formulation that utilizes the enthalpy method for phase change. The phase change process for the tube bank is coupled with the conservation of energy to determine the bulk HTF temperature exiting each column of tubes and ultimately the tube bank. Experimentation has been performed for model validation, and the transient numerical simulation results are compared with the experimental findings.

CHAPTER 2

NUMERICAL SIMULATION

The numerical simulation contains two primary components – the PCM-filled tube component and the HTF component. These components are coupled together via energy conservation to comprise the full simulation.

2.1 The PCM-Filled Tube Component

The following assumptions were made for the numerical analysis of the PCM-filled tubes:

- Conduction is the only mode of heat transfer considered in the PCM.
- The thermophysical properties of the PCM and cylindrical tubes are independent of temperature, but solid and liquid PCM phases maintain different properties.
- Phase change occurs for the PCM at a single temperature.
- The PCM and tubes are both homogeneous and isotropic.
- The initial PCM and tube temperatures are uniform.

The energy conservation equation for one-dimensional radial phase change with constant thermophysical properties can be expressed in terms of total volumetric enthalpy and temperature:

$$\frac{\partial H}{\partial t} = \frac{1}{r}\frac{\partial}{\partial r}\left(kr\frac{\partial T}{\partial r}\right) \tag{1}$$

where total volumetric enthalpy is the sum of sensible and latent heats:

$$H(T) = h(T) + \rho f(T) L \tag{2}$$

and

$$h(T) = \int_{T_m}^{T} \rho_k C_k dT \tag{3}$$

The liquid fraction of melt is defined as follows for isothermal phase change:

$$f = \begin{cases} 0 & \text{if } T < T_m \quad \text{(solid)} \\ 0 - 1 & \text{if } T = T_m \quad \text{(mushy)} \\ 1 & \text{if } T > T_m \quad \text{(liquid)} \end{cases} \tag{4}$$

From Eqs. (2), (3), and (4), the total volumetric enthalpy is found to be

$$H = \begin{cases} \int_{T_m}^{T} \rho_s C_s dT & \text{if } T < T_m \quad \text{(solid)} \\ \rho f L & \text{if } T = T_m \quad \text{(mushy)} \\ \int_{T_m}^{T} \rho_l C_l dT + \rho_l L & \text{if } T > T_m \quad \text{(liquid)} \end{cases} \tag{5}$$

Equations (2) and (3) are used to obtain another version of Eq. (1) in terms of specific enthalpy for the PCM

$$\frac{\partial h}{\partial t} = \frac{1}{r}\frac{\partial}{\partial r}\left(\alpha r \frac{\partial h}{\partial r}\right) - \rho L \frac{df}{dt} \tag{6}$$

and for the cylindrical tubing

$$\frac{\partial h_{ct}}{\partial t} = \frac{1}{r}\frac{\partial}{\partial r}\left(\alpha_{ct} r \frac{\partial h_{ct}}{\partial r}\right) \tag{7}$$

Equations (6) and (7) are solved with a fully-implicit approach. As performed by Patankar [36], the integration of Eqs. (6) and (7) over each control volume produces the finite volume equation in Eq. (8) for the PCM, and the equivalent for the cylindrical tubing but without the latent heat. Figure 2.1 illustrates the placement of control volumes and the radial positioning of the nodes and interfaces, where W, P, and E represent the west, center, and east nodal locations, respectively, and w and e represent the west and east interface locations, respectively.

$$r_P h_P = r_P h_P{}^{o} + R[r_e h_e \alpha_e + r_w h_w \alpha_w - (r_e \alpha_e + r_w \alpha_w) h_P] + r_P \rho L (f_P{}^{o} - f_P{}^{k}) \tag{8}$$

or

$$a_P h_P + a_E h_E + a_W h_W = Q \tag{9}$$

where

$$a_P = r_P - a_E - a_W, \quad a_E = -\alpha_e R r_e, \quad a_W = -\alpha_w R r_w$$

$$Q = r_P\left[h_P{}^o + \rho L\left(f_P{}^o - f_P{}^k\right)\right], \quad R = \frac{\Delta t}{(r_e - r_w)^2}$$

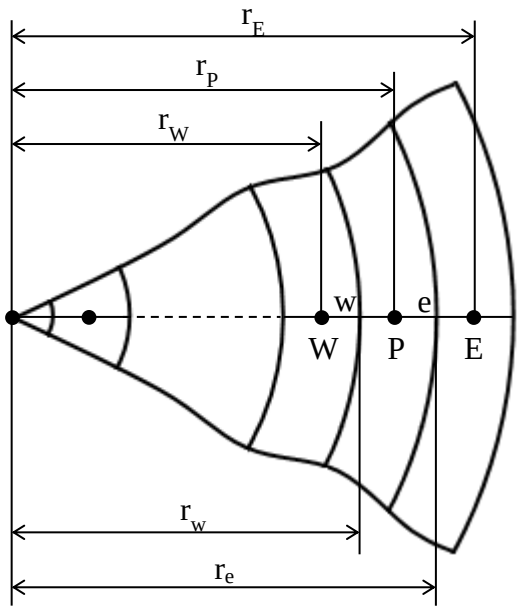

Figure 2.1: Control Volumes and Radial Positioning of Nodes and Interfaces

The values $h_P{}^o$ and $f_P{}^o$ refer to the enthalpy and liquid fraction of melt of node P, respectively, from the previous time step. The value $f_P{}^k$ is the liquid fraction of melt of node P on the k^{th} iteration. Q is the source term that keeps track of the change in latent heat per iteration.

Equation (9) is solved with a Tri-Diagonal Matrix Algorithm (TDMA). The liquid fraction of melt is then updated, per the method suggested by Voller [37]. Here, if a node shows $0 < f < 1$, phase change is known to be occurring; a_P is then set to a very large

number (10^{15} in the present study), and $h_P$is set to zero, since $T = T_m$. Equation (9) is rearranged to be

$$f_P{}^{k+1} = f_P{}^{o} + \frac{-a_P h_P - a_E h_E + r_P h_P{}^{o}}{r_P \rho L} \tag{10}$$

and then Eq. (10) is used at each node, followed by an under/over correction:

$$f = \begin{cases} 0 & \text{if} \quad f_P{}^{k+1} \leq 0 \\ 1 & \text{if} \quad f_P{}^{k+1} \geq 1 \end{cases}$$

Convergence at a time step is obtained when the total enthalpy change falls below a prescribed tolerance:

$$\frac{ABS(H^k - H^{k+1})}{\rho_k C_k} < TOL \tag{11}$$

The present study sets TOL to 10^{-4}. A thorough handling of phase change with the enthalpy method in Cartesian coordinates can be found in the study by Costa et al. [38].

When simulating a domain with multiple materials of different thermal conductivities, it is necessary to define an interface thermal conductivity that ensures heat flux continuity. This is also necessary if the PCM has differing thermal conductivities in the solid and liquid phases. The interface thermal conductivity for k_e, for example, can

be found by setting the thermal resistance from P to E equal to the combined thermal resistance from P to e plus e to E, as in Eq. (12).

$$\frac{\ln\left({}^{r_E}/_{r_P}\right)}{k_e} = \frac{\ln\left({}^{r_e}/_{r_P}\right)}{k_P} + \frac{\ln\left({}^{r_E}/_{r_e}\right)}{k_E} \tag{12}$$

This results in the interface thermal conductivity:

$$k_e = \frac{\ln\left({}^{r_E}/_{r_P}\right)}{\frac{\ln\left({}^{r_e}/_{r_P}\right)}{k_P} + \frac{\ln\left({}^{r_E}/_{r_e}\right)}{k_E}} \tag{13}$$

Figure 2.2 illustrates how the phase change model progresses through the melting process. The blue volumes represent solid PCM control volumes at the melting temperature, and a volume that is a lighter shade of blue represents the control volume currently undergoing melting. Upon fully melting, a control volume quickly rises in temperature via sensible heat, allowing the following control volume to begin melting.

The PCM-filled tube simulation component has been validated using two results from the literature. Voller and Cross [39] performed numerical simulations to determine the total solidification time for a cylinder of PCM with a uniform wall temperature boundary condition. PCM values and boundary conditions were chosen for the present study to correspond with Voller's and Cross' dimensionless values. Table 2.1 gives one set of these validation test specifications listed as Test 1.

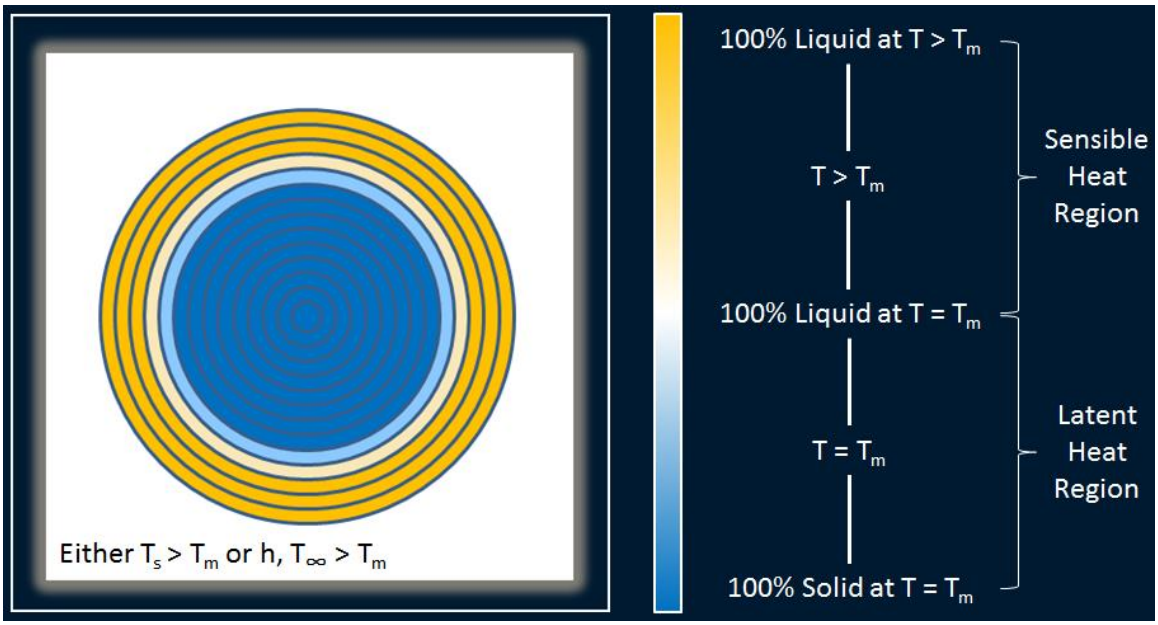

Figure 2.2: Polar Model Phase Change Illustration

Table 2.1: Properties and Conditions for Single Cylinder Numerical Validation

Property or Condition	Test 1	Test 2
Cylinder radius (mm)	46.2	20
Boundary Condition	T_w = 290 K	HTC = 500 W/m^2-K T_{air} = 290 K
PCM		
Initial temperature (K)	302	300
Freezing temperature (K)	300	298
Density (kg/m^3)	1480	1000
Latent heat (kJ/kg)	300	100
Specific heat (kJ/kg-K)	1.5	5.0
Thermal conductivity (W/m-K)	0.733	2.0

The solution by Voller and Cross gave the total time for solidification to be 9.318 hours, and the model used in the present study gave a total time of 9.314 hours, only 0.05% difference. Comparing the results from nine cases provided by Voller and Cross, the average percent difference with their results was 0.33%. Figure 2.3 shows the transient temperature profiles of the PCM at various radial positions within the PCM

cylinder. The outermost control volume freezes first, followed by its adjacent control volume, and so forth, until the center node fully freezes.

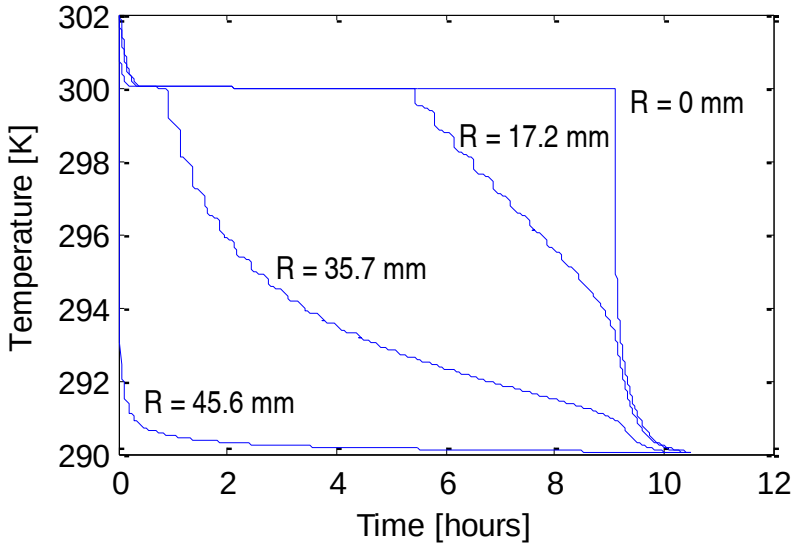

Figure 2.3: Radial Transient Temperature Profiles

The model was also validated for the convective boundary condition with Teggar et al. [40]. Again, PCM values and boundary conditions were chosen to correspond with dimensionless values, listed as Test 2 in Table 2.1. They studied the melting in three different PCM capsules, and while an exact melting time is not given, a plot of the temperature of the PCM center over time is provided. A test was performed, and the results from this study's numerical simulation, shown in Figure 2.4, have been placed along results from Teggar et al. for comparison. The blue line represents the transient temperature of the center of a PCM cylinder from the present study, and the dashed red line represents the transient temperature of the center of the cylinder from Teggar et al.

The PCM cylinder begins at a uniform initial temperature of 300 K, and when the convective boundary condition is applied, the temperature of the PCM drops. The

outermost control volume freezes first, and then the second, and so forth until the center control volume freezes. At this point the latent heat of the PCM has been fully expended, and the center control volume of the PCM quickly drops in temperature, following the manner of the outer nodes.

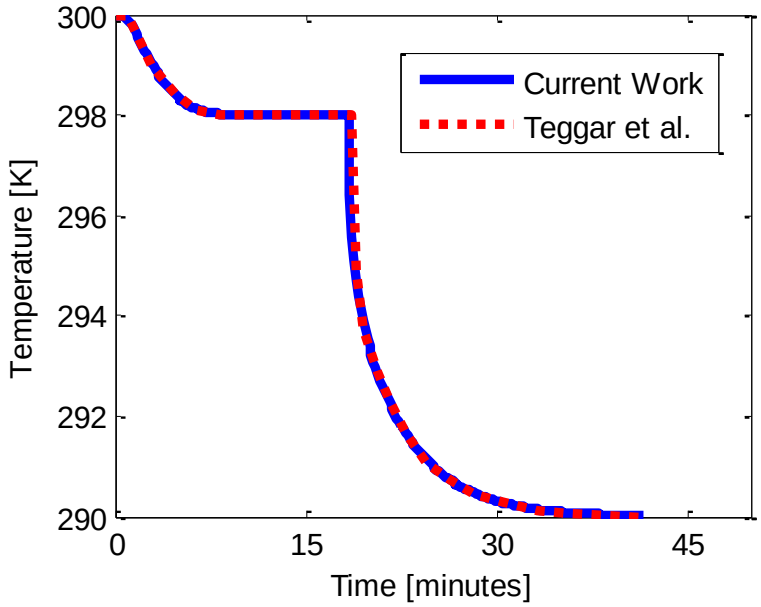

Figure 2.4: Validation of Single Cylinder Numerical Model with Convective Boundary

2.2 The HTF Component

The following assumptions were made for the analysis of the HTF component:

- The HTF flowing over the tube bank is considered to have a uniform bulk temperature for each individual column of tubes, meaning that each tube within a column will exhibit the same rate of energy storage or loss.

- The HTF has a uniform initial temperature equal to that of the PCM and tubes. At the start of the simulation, HTF of a prescribed temperature enters the TES unit, and this inlet temperature is maintained as the inlet condition throughout the simulation.

A global energy balance is performed on the system using the control volumes shown in Figure 2.5, coupled with the numerical phase change model. If two control volumes are considered, as in Figure 2.6, water is seen to enter the first column at a certain temperature, and that temperature is used as that column's local ambient temperature. An energy balance is performed on one PCM cylinder in the column and multiplied by the number of cylinders in that column; the energy gained by the PCM is lost by the water, or vice versa. An exit water temperature from that control volume is found and used as the inlet water temperature for the next column during the next time iteration. The water temperature is tracked along the length of the tube bank for the entire simulation. The following energy balance equation is employed:

$$\dot{m}C_{HTF}(T_n - T_{n+1}) = Nm_{ct}C_{ct}\frac{\Delta T_{ct}}{\Delta t} + NL\frac{m_{melt}}{\Delta t} + Nm_sC_s\frac{\Delta T_s}{\Delta t} + Nm_lC_l\frac{\Delta T_l}{\Delta t} \qquad (14)$$

where N is the number of tubes in a column, and n is the column in consideration. The time step is chosen based upon the amount of time required for the given flow rate to move fluid from one HTF control volume to the next.

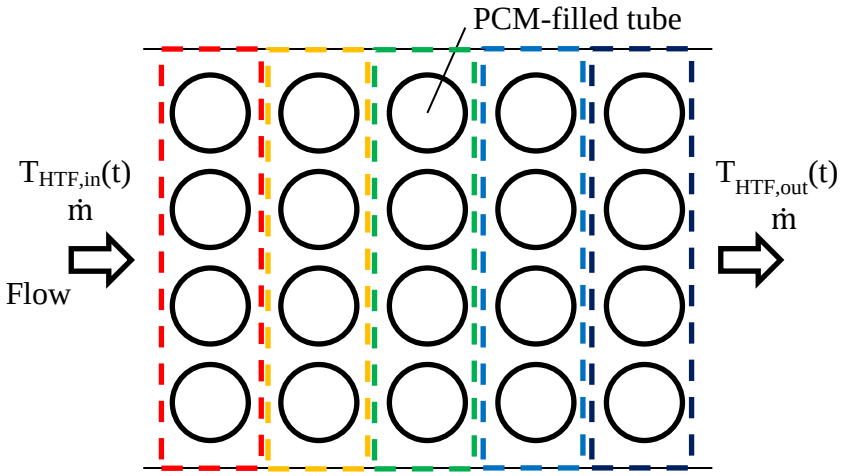

Figure 2.5: Control Volumes within TES Unit for Global Energy Balance

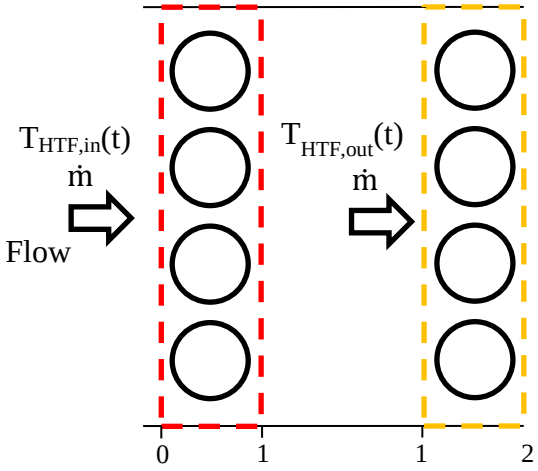

Figure 2.6: Control Volume Illustration for Coupling the PCM Tube Model with HTF

2.3 The Conduction-Dominated Heat Transfer Assumption

To determine the reasonableness of the conduction-dominated heat transfer assumption, numerical results by Chung et al. [41] were examined. At low Rayleigh numbers, convection plays a minor role in the melting within a cylinder, but at high

Rayleigh numbers, convection plays a very significant role. Figure 2.7 shows their results for Ra = 1.0×10^4 at two dimensionless time values, and the solid-liquid interface remains nearly concentric throughout the melting process, indicating little effects from convection. The left half of each cylinder in the figure shows the isotherms, and the right halves show the velocity contours. Figure 2.8 shows their results for Ra = 3.6×10^5, and the solid-liquid interface is seen to be changing more drastically compared to the results with a smaller Rayleigh number due to increased convection.

Figure 2.7: The Isotherms (left) and Velocity Contour (right) at Ra = 1.0×10^4, Ste = 0.045, and Sc = 0.004 [41]

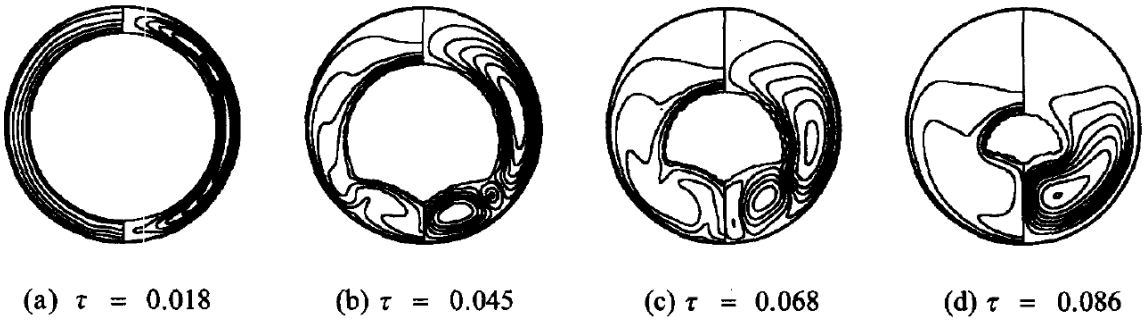

Figure 2.8: The Isotherms (left) and Velocity Contour (right) at Ra = 3.6×10^5, Ste = 0.045, and Sc = 0.004 [41]

While the experimental results of the present study have yet to be discussed in this paper, it is important to note here that the largest Rayleigh number in the present study, based upon a wall temperature rise of 8 K above the PCM melting temperature, is 8.3×10^4. This value falls between the two results formerly referenced, and is fairly closer to the smaller of the two.

CHAPTER 3

EXPERIMENTAL SETUP AND PROCEDURE

3.1 Detailed Description of Flow Loop Setup

The experimental setup used for validating the numerical model is shown as a schematic in Figure 3.1, and a picture of the system is provided in Figure 3.2. The primary components of the experimental flow loop are a thermostatic bath, two gear pumps, a flow meter, the TES unit, a cold plate with attached thin-film heaters, and copper-constantan (T-type) thermocouples of wire diameter 0.25 mm. To illustrate the thermal changes in the water through the flow loop, the temperature change of the flow through the system is shown in Figure 3.3, with red representing hot water and blue representing cold water. Details of the system flow loop are provided in the coming subsections. The details of the TES setup are discussed in the following section.

3.1.1 Thermostatic Bath

To provide water at a constant temperature to the TES unit inlet, a Thermo Scientific Haake AC150-A25 bath circulator, shown in Figure 3.4, was employed. This thermostatic bath was essential for maintaining a constant water inlet temperature to the TES unit throughout experimentation such that the experimental findings could be properly compared with the numerical results. The thermostatic bath's total fill volume is twelve liters.

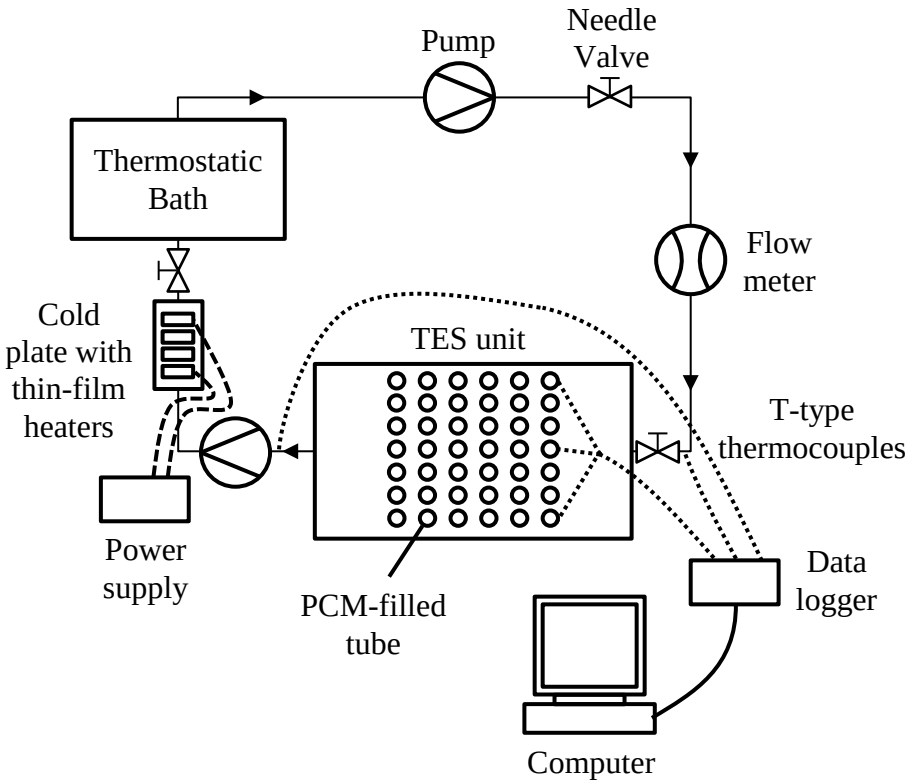

Figure 3.1: Experimental Schematic

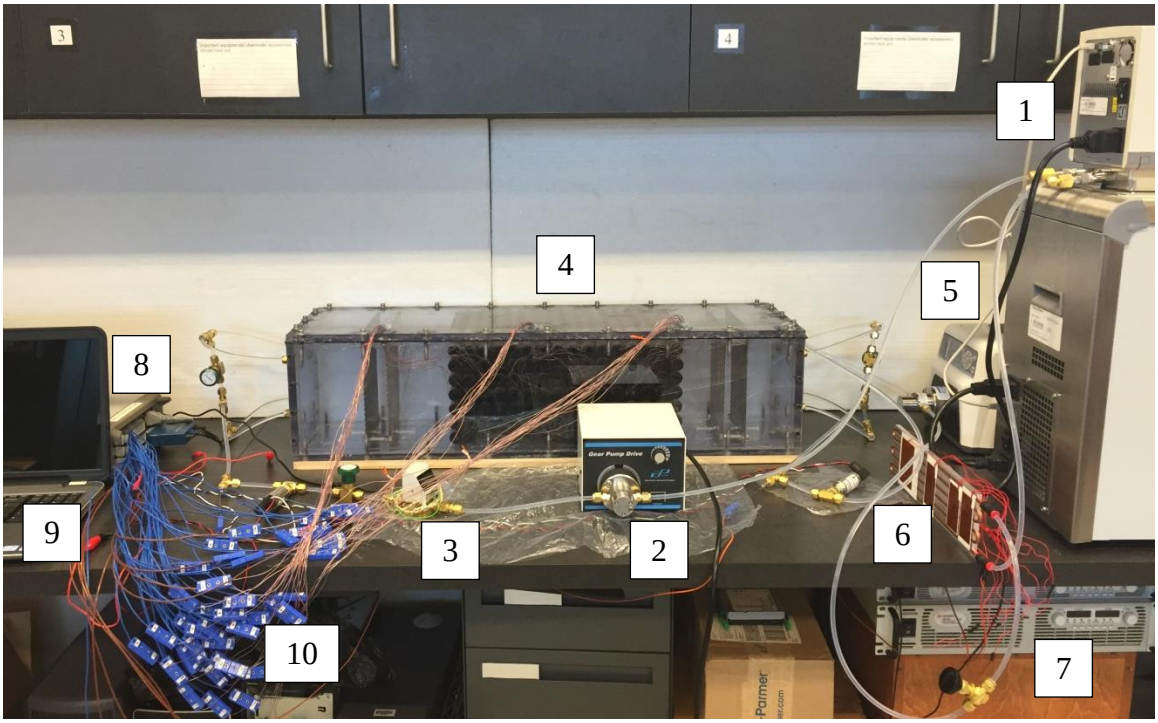

1 – Thermostatic bath
2 – Gear pump
3 – Flow meter
4 – TES unit
5 – Gear pump
6 – Cold plate with attached heaters
7 – Power supplies
8 – Data acquisition system
9 – Computer
10 – TES thermocouple wires

Figure 3.2: Experimental Setup

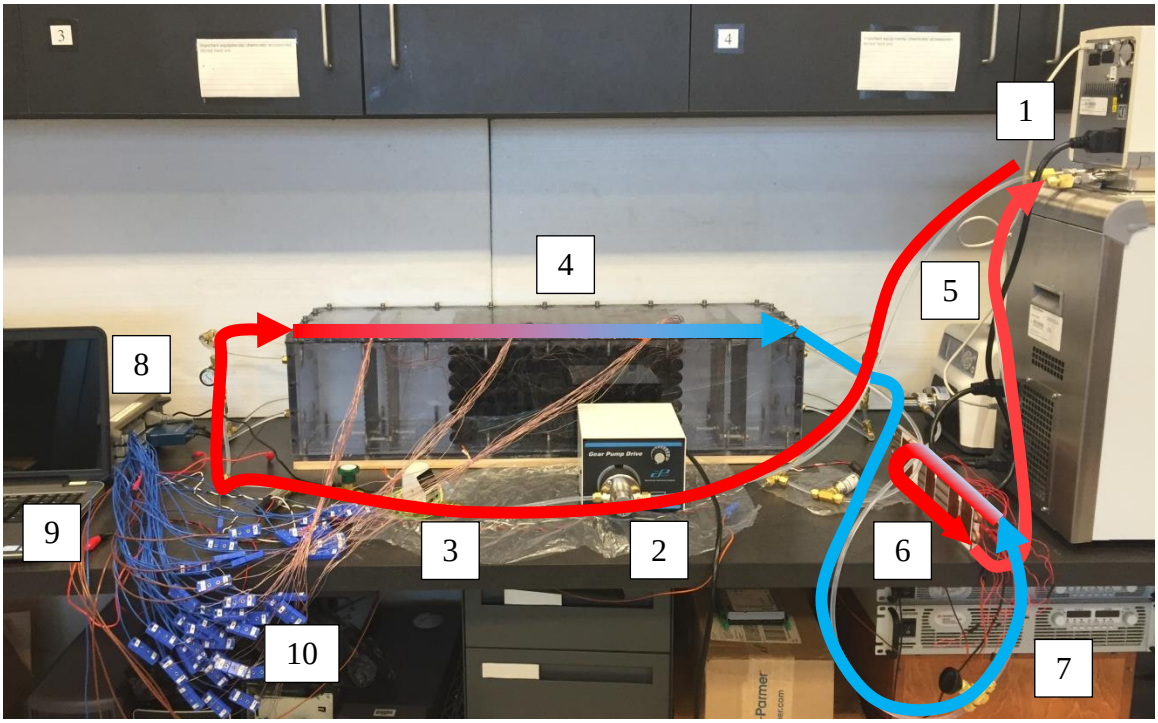

1 – Thermostatic bath
2 – Gear pump
3 – Flow meter
4 – TES unit
5 – Gear pump
6 – Cold plate with attached heaters
7 – Power supplies
8 – Data acquisition system
9 – Computer
10 – TES thermocouple wires

Figure 3.3: Temperature of Flow through Experimental Setup

Figure 3.4: Thermo Scientific Haake AC150-A25 Bath Circulator

3.1.2 Gear Pumps

To adjust the fluid flow into the TES unit, a Cole-Parmer Console Drive EW-75211-10 with a Micropump A-Mount Cavity Head EW-07001-40, shown in Figure 3.5, was used. With this pump head, the pump is capable of producing smooth flow between 45.5 mL/min to 4550 mL/min. At flow rates above 1.0 L/min, it was necessary to add another pump to the flow loop at the outlet of the TES unit to draw water from the TES unit at the same rate it was entering. A Cole-Parmer Digital Drive EW-75211-70 with a Micropump A-Mount Cavity Head EW-74012-21, together capable of producing smooth flow between 23.04 mL/min to 2304 mL/min, was used for this purpose and is shown in Figure 3.6.

Figure 3.5: Gear Pump at TES Inlet

Figure 3.6: Gear Pump at TES Outlet

3.1.3 Flow Meter

The flow rate of water through the system was measured by a McMillan Model S-112-9-D-B6 flow meter, shown in Figure 3.7, with the capacity to measure volumetric flow up to 10.00 L/min. Because flow rate plays an important role in the experimental results, an accurate measurement of this value is crucial; the full scale accuracy (including linearity) of this flow meter is ±1.0%.

Figure 3.7: McMillan Model S-112-9-D-B6 Flow Meter

3.1.4 Cold Plate

At the beginning of an experimental run, the temperature of the water and PCM within the TES unit was at a uniform temperature equal to that of their environment (21-23 °C), ten or more degrees lower than the water exiting the thermostatic bath. Because of this difference in temperature, the thermostatic bath is unable to maintain the desired bath temperature. Thin-film heaters were attached to a cold plate to provide sufficient

heat to the water after exiting the TES unit to alleviate the load on the thermostatic bath. The Lytron CP15G05 tubed cold plate with a six-pass configuration and a 12 in. × 3.75 in. mounting surface was used to transfer the heat from the thin-film heaters to the water.

3.1.5 Thin-Film Heaters

Using four Minco thin-film heaters (HK5456R82.9L12A) of 82.9 Ω and one Minco thin-film heater (HK5376R92.1L12A) of 92.1 Ω in series on one side of the cold plate, a combined heater resistance of 423.7 Ω was established. Three thin-film heaters (HK5376R92.1L12A) of 92.1 Ω and one heater (HK5170R123L12A) of 123 Ω for a combined resistance of 399.3 Ω were placed on the other side of the cold plate. Having no adhesive backing on the heaters themselves, Cool Bond PSA-3NC high thermal conductivity tape was used to attach the heaters to the cold plate. One side of the cold plate and its attached heaters are shown in Figure 3.8.

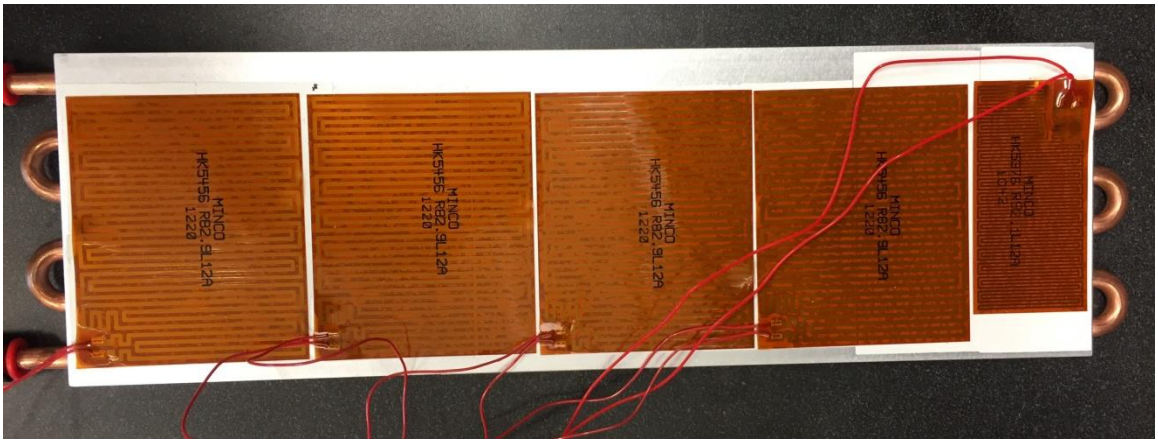

Figure 3.8: Thin-film Heaters attached to Cold Plate

3.1.6 Power Supplies

An Agilent N5752A System DC Power Supply and a Keysight Technologies N8731A-42A System DC Power Supply were employed to supply power to the thin-film heaters. Able to output up to 600 V and 1.3 A, the Agilent power supply is capable of supplying up to 780 W of power to the thin-film heaters, and the Keysight power supply is capable of providing up to 3.3 kW of power at 600 V and 5.5 A. When performing an experiment, the power supplies were adjusted as the difference in the thermostatic bath temperature (which needed to remain constant) and the exit fluid temperature from the TES unit decreased.

3.1.7 Data Acquisition System

To collect and record the temperatures within the flow loop and the TES unit, an Agilent 34970A Data Acquisition / Data Logger Switch Unit was utilized. Three Agilent 34901A Multiplexer Modules with twenty channels each were used to connect the thermocouples to the data acquisition system, and these modules have a built-in thermocouple reference junction.

3.1.8 Thermocouples

Other than the thermocouples within the TES unit, two thermocouples were placed in the flow loop, one before the TES inlet and one after the TES exit. These ungrounded, sheathed T-type thermocouples (TMQSS-062U-6) were inserted into the flow to measure the temperature of the fluid entering and exiting the TES unit. These thermocouples were

calibrated using an Omega Model CL122 dry block calibrator and the data acquisition system. The thermocouples within the TES unit were calibrated in like manner.

3.2 Detailed Description of TES Unit Setup

The TES unit was carefully designed to ensure that the experimental findings could be reasonably compared to the numerical results. The TES unit measured 0.91 m long, 25.4 cm wide, and 22.9 cm high and was comprised of 1.27 cm thick polycarbonate sheets, PCM-filled tubes, and baffles for flow distribution. The baffles are placed between the unit's inlet and the tube bank, as well as between the tube bank and the unit's outlet. To promote even flow distribution further, the flow was split into four streams immediately before entering the TES, and the flow exited the TES in four streams before quickly being joined together again. Figure 3.9 shows the fully assembled TES unit with fluid flow from left to right. Figure 3.10 shows the TES unit inlet, where four evenly distributed inlet ports exist for the inlet flow.

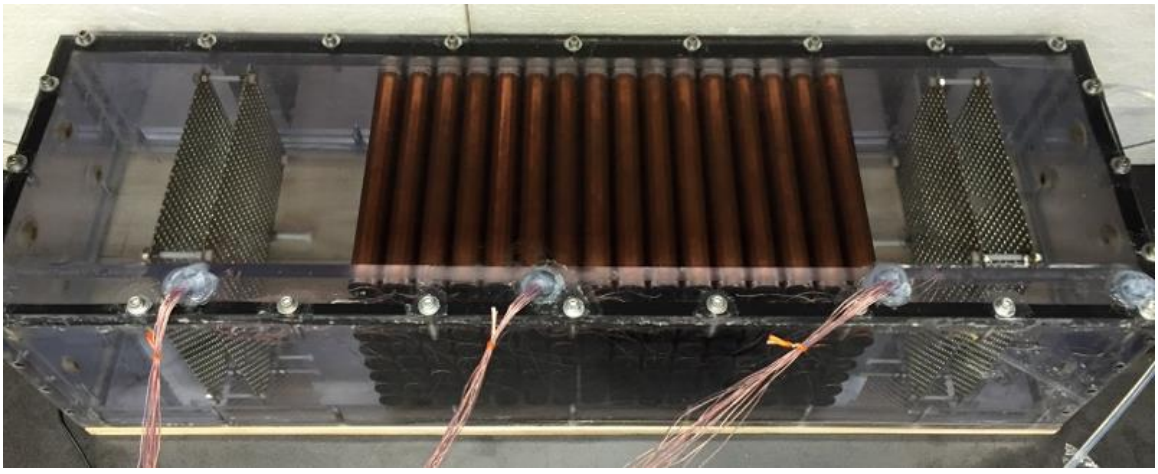

Figure 3.9: Thermal Energy Storage Unit

Figure 3.10: TES Unit Inlet

3.2.1 Baffles for Flow Distribution

Because evenly distributed flow in the experimental TES unit is crucial for numerical validation, 20.32 cm × 20.32 cm (8 in. × 8 in.) baffles were placed between the TES inlet and the tube bank, as well as between the tube bank and the TES outlet. For each baffle two stainless steel perforated plates were offset from one another by 1.5 in. with bolts and nuts securing them in position. Four thermocouples were placed on each set of baffles to determine the temperature uniformity of the flow. The thermocouples were placed approximately 1.5 in. from the edge of the baffles and 1 in., 3 in., 5 in., and 7 in. from the bottom of the baffles. The baffle is shown in Figure 3.11.

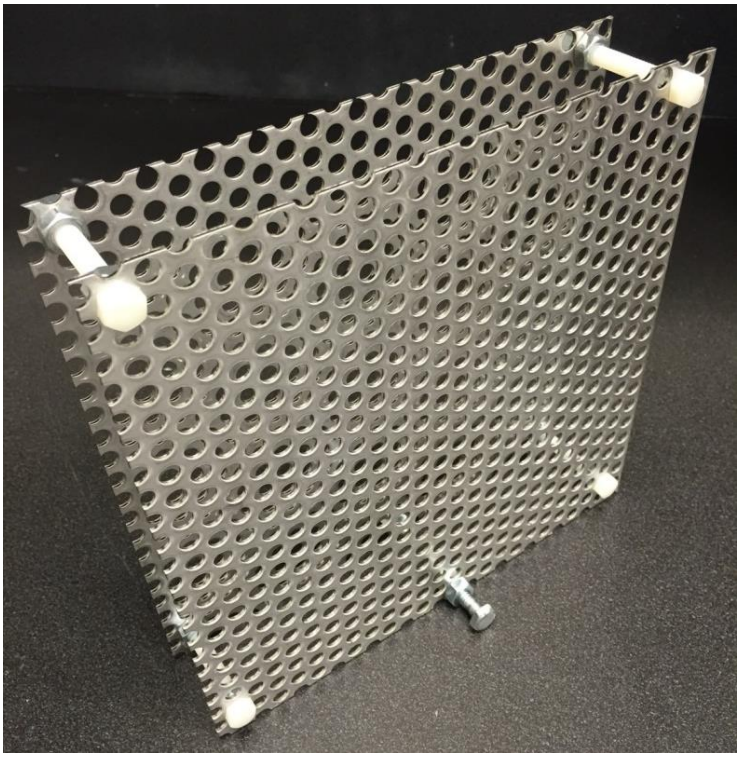

Figure 3.11: Perforated Plate Baffle

3.2.2 PCM-Filled Tubes

The design of the TES unit required the careful consideration of several factors. Firstly, Rubitherm RT 28 HC paraffin PCM was decided upon for its suitable melting temperature and its very high latent heat of fusion. The properties of RT 28 HC are given in Table 3.1. The value for the liquid thermal expansion coefficient could not be found in the literature for RT 28 HC, so the value found for RT 27 has been given in the table as the closest available value. Because the numerical model requires one value for PCM melting temperature and one value for density, a melting temperature of 28 °C and a density of 825 kg/m3 have been used. The properties of copper used in simulation are listed in Table 3.2, and the specific heat used for water was 4.179 kJ/kg-K.

Table 3.1: Thermophysical Properties of Rubitherm RT 28 HC [42]

RT 28 HC	Value
Melting/Freezing temperature	27-29°C
Latent heat	~245 kJ/kg
Density (solid)	880 kg/m^3
Density (liquid)	770 kg/m^3
Specific heat (solid and liquid)	2.0 kJ/kg-K
Thermal conductivity (solid and liquid)	0.2 W/m-K
Kinematic viscosity	3.1×10^{-6} m^2/s [43]
Liquid thermal expansion coefficient (β)	0.0005 K^{-1} [44]

Table 3.2: Thermophysical Properties of Copper

Copper	Value
Density (kg/m^3)	8960
Specific heat (kJ/kg-K)	0.3844
Thermal conductivity (W/m-K)	401

Concerning the tube material, it was decided that copper would be used because of its high thermal conductivity, which would reduce charging and discharging times. The size of the copper tubes was chosen based on the desire to have relatively small volumes of PCM encapsulated in the tubes and the ability to have numerous columns of tubes without necessitating an enormous TES unit. Using the numerical model, the number of rows and columns in the tube bank was decided upon such that a noticeable drop in water temperature from the TES inlet to outlet could be observed. Knowing that densely packed tubes generally increases the average heat transfer coefficient of the tube bank, the tubes were spaced closely together, and polycarbonate sheets were used within the unit to support the tubes. The mass of each was measured before and after the PCM-filling

process, to within a tenth of a gram, to determine the total mass of PCM within the tube bank. The details of the experimental configuration are provided in Table 3.3.

Table 3.3: Details of Experimental Configuration

Tube Bank Arrangement	Value
Number of columns	16
Number of rows	7
Tube size	3/4 in. ID, 7/8 in. OD
Total tube length	22.9 cm (9 in.)
PCM length in tube	17.86 cm
Total PCM mass	4.641 kg
S_T and S_L	2.667 cm (1.05 in.)

3.2.2.1 PCM Tube-Filling Process

The low ambient temperature chamber in the Sustainable Thermal Systems Laboratory was used to maintain a chamber temperature at approximately 99°F (37.2°C) for melting the PCM for the tube-filling process. While the PCM melts at 28°C, this higher temperature was used such that the PCM would be in its least dense (most expanded) state during the filling process, meaning that upon future melting at temperatures less than 37.2°C, the PCM would theoretically not leak due to thermal expansion. Each tube was manually filled in this environment.

First, a rubber seal plug was inserted at the end of a tube, and the tube was temporarily set aside. Then, a small capillary tube was forced through the center of another rubber seal plug, as seen in Figure 3.12, and then this was set aside.

Figure 3.12: Capillary Tube within Seal Plug for Sealing Process

Next, the tube was slowly filled by pouring the liquid PCM into the tube, which was angled during the pouring process to prevent entrapment of air. Upon filling the tube to the very top, the rubber seal plug with the capillary tube was forced onto the other end of the tube; during the insertion of this rubber seal plug, liquid PCM was forced out of the capillary tube. The capillary tube was then removed, and because of the density of the rubber, the space that the capillary tube temporarily occupied was filled back by the rubber. Silicone was still placed in the cavity of the rubber seal plug for precautionary measure.

3.2.2.2 Thermocouple Insertion within Tubes

T-type 30 AWG thermocouples (Omega 5TC-TT-T-30-36) were placed in the radial and approximate length-wise center of many PCM-filled tubes. To place thermocouples in the center of the tubes, a structure comprised of stainless steel washers and capillary tubes was designed. It was crucial that this structure maintain the position of the thermocouple while not requiring excessive space within the tube.

First, an approximately 4.5 inch long stainless steel capillary tube of 0.052” ID and 1/16” OD was forced into a rubber seal plug. Then, a stainless steel washer (0.064” ID and only a few thousandths of an inch smaller in outer diameter than the inner diameter of the copper tube) was placed on the capillary tube to maintain the radial position of the capillary tube within the copper tube. Each washer used in these tubes had been cut on either side of its inner hole such that its outer edge was no longer circular but had two curved portions and two straight parallel portions; these cuts were made such that air would not get trapped beneath the washers when pouring PCM in the tubes. Then, a one inch capillary tube of 0.074” ID and 3/32” OD was placed on the former capillary tube to act as a spacer. Another washer was then placed on the first capillary tube, separated one inch from the first washer by the spacer. The tip of the thermocouple wire was fed through the first capillary tube at the end where it sat in the rubber stopper until the tip of the thermocouple protruded slightly from the end of the capillary tube. Fast-curing epoxy was then used to seal the stopper and secure the structure and the thermocouple in place, while taking care to prevent the epoxy from contacting the thermocouple tip. The stopper and the structure were finally inserted into the copper tube, and the PCM-filling process was carried out in the same way as done for the non-instrumented tubes. Figure 3.13 shows the finalized structure before inserting the thermocouple and adding epoxy, and Figure 3.14 shows the machined washer used to place the capillary tube at the radial center.

Figure 3.13: Structure for Maintaining Thermocouple Placement within Tubes

Figure 3.14: Machined Washer for Thermocouple Structure

3.2.2.3 Thermocouple Placement on Tubes

T-type thermocouples were also placed on the surface of several copper tubes. For each of these tubes, a small groove was drilled halfway along the length of the tube for the thermocouple wire to be placed. Thermally conductive OMEGABOND epoxy adhesive with a thermal conductivity of 1.04 W/m-K was used to cover the space between the thermocouple wire and the copper tube, along the length of the wire and also at the tip. The excess epoxy was removed to ensure a relatively smooth surface. Figure 3.15 shows the placement of the thermocouple wire and thermal epoxy on the copper tube.

Figure 3.15: Thermal Epoxy Applied for External Thermocouple Placement

3.2.2.4 Thermocouple Placement within TES Unit

The instrumented tubes were placed within the tube bank in an arrangement such that the uniformity of the flow distribution could be determined by the experimental results. By placing instrumented tubes in the top, middle, and bottom rows, flow distribution would be known to be uniform if the thermocouples in the top, middle, and bottom tubes within a column recorded similar temperature profiles. Figure 3.16 illustrates the thermocouple placement within the tube bank. Blue circles represent tubes with a thermocouple placed at their center, and blue-gold striped circles represent tubes with a thermocouple placed on the tube's surface as well as at their center.

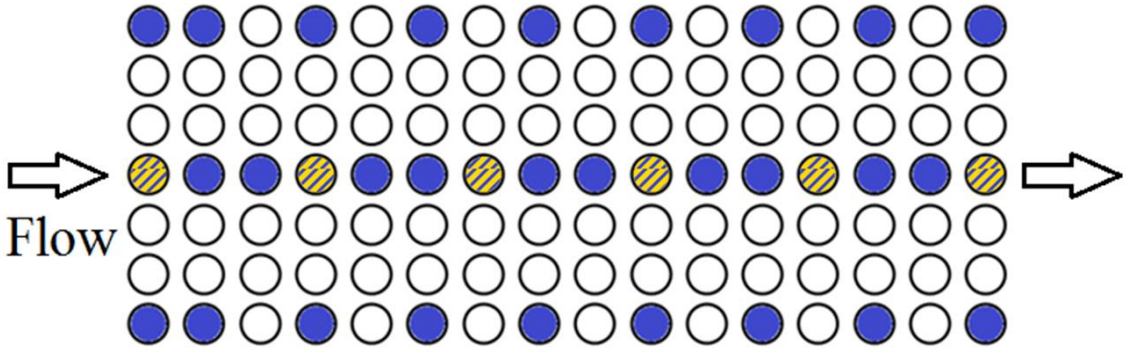

Figure 3.16: Thermocouple Placement within Tube Bank

3.2.3 Tank Filling and Sealing

Upon placing the PCM-filled tubes into the support structures and down into the tank, deionized water was poured into the tank until the water reached approximately one inch from the top of the tank. After leaving the tank in this mostly-filled state for a day, a significant number of bubbles formed on the tubes and walls within the unit; these bubbles were then manually dislodged, and they did not return.

Before the lid was fully screwed into the tank, it was necessary to bring the thermocouple wires up through holes placed in the lid. After doing so the lid was screwed down onto the tank body, compressing a rubber EPDM gasket placed between the two to prevent leakage. To prevent water from exiting through the holes in the lid, rubber stoppers were used to fill the holes; a small hole was drilled into each rubber stopper to allow the thermocouple wires to exit the tank through those holes. This process was done for three of the four holes in the lid, and one hole was left for filling the tank with water. The rubber stoppers fit securely in the holes, leaving only the holes in the stoppers themselves as potential places for leakage. 100% silicone waterproof adhesive sealant was used to fill the hole in each rubber stopper, and the silicone was added around the top of the rubber stoppers as well to prevent leakage in case they were not perfectly positioned in the holes. Furthermore, silicone was also added around the sides where the lid, gasket, and tank interfaced to ensure complete sealing.

After sealing the TES unit, apart from the one remaining hole in the lid, the tank was filled with water the remainder of the way by closing the needle valve between the outlet of the TES unit and the thermostatic bath, turning on the thermostatic bath, and pumping water to the tank slowly. The tank sat atop a slightly angled wooden board

which caused the unit to sit at a very slight incline, thereby forcing air out of the remaining hole in the lid, leaving an insignificant amount of air trapped at the top of the tank. A rubber stopper with a small hole in it was placed in the final hole of the lid. This hole in the stopper was partially covered to prevent evaporation losses during testing, but it was intentionally left unsealed. With the placement of gear pumps at the inlet and outlet of the TES unit, it was noticed that if the tank was completely sealed, any difference in produced flow rate between the two pumps would lead to expansion of the tank, contraction of the tank, or forced leakage from the tank. By leaving this single hole unsealed at the highest point in the tank, the water level within the tank could be closely monitored throughout an experiment to ensure the TES unit was nearly full, without a rising or receding water level.

3.3 Experimental Procedure

Before beginning the experimental discharging process, the thermostatic bath was programmed to maintain the bath's water temperature at a desired value higher than the PCM's melting temperature. The discharging process was begun by initiating flow from the thermostatic bath to the pump, which circulated the fluid to the TES unit and through the flow loop. The experimental TES unit was considered fully charged when every instrumented tube was fully melted; tubes were reasoned to be fully melted when the thermocouples placed in their centers revealed temperatures greater than the PCM's melting temperature. It was observed both experimentally and numerically that the temperature of the center of the PCM-filled tube rises rapidly after remaining at a

relatively constant temperature for a lengthy time; this notably fast rise in temperature is associated with full melting at the tube center.

A variety of experiments were performed to assess the effects of differing HTF inlet temperatures and flow rates. Thermocouples measured the temperature in selected tubes, at the inlet and outlet of the TES unit, and at set locations on the baffles, and they were recorded every ten seconds by the data acquisition system. The HTF flow rate was monitored by a flow meter.

CHAPTER 4

NUMERICAL AND EXPERIMENTAL RESULTS

In order to evaluate the accuracy of the numerical model, several experiments were performed with different HTF inlet temperatures and flow rates. The heat transfer coefficients used in the numerical model were average tube bank values based upon the correlation by Zukauskas [45]. Because the numerical model, as presented previously, does not consider any water prior to or after the tube bank, the model was modified to ensure realistic comparisons between the numerical and experimental results.

4.1 Numerical Model Adjustment

Because a large volume of water precedes the inlet water's entrance to the tube bank (~10.92 L), a transient control volume energy conservation equation was employed to characterize the transient temperature of the water entering the tube bank. Equations (15-18) show the steps taken to produce the first-order ordinary differential equation, where T is the bulk water temperature and the exit temperature of the water from the control volume. The solution assumes perfect mixing within the control volume.

$$\frac{dE_{HTF}}{dt} = \dot{m}(h_{HTF,in} - h_{HTF}) \tag{15}$$

$$m\frac{du_{HTF}}{dt} = \dot{m}C(T_{HTF,in} - T_{HTF}) \tag{16}$$

$$mC\frac{dT_{HTF}}{dt} = \dot{m}C(T_{HTF,in} - T_{HTF}) \tag{17}$$

$$\frac{dT_{HTF}}{dt} = \frac{\dot{m}}{m}(T_{HTF,in} - T_{HTF}) \tag{18}$$

Solving Eq. (18) as a first-order ordinary differential equation with $T(t=0) = T_o$, the following exact solution is found:

$$T_{HTF}(t) = T_{HTF,in}\left(1 - e^{\frac{-\dot{m}}{m}t}\right) + T_o e^{\frac{-\dot{m}}{m}t} \tag{19}$$

Because there is a large volume of water after the tube bank (~8.17 L), it is necessary to employ this adjustment to the water exiting the tube bank as well. Since, however, the temperature of the water exiting the tube bank changes with time, a numerical solution is employed, rather than the exact solution. Equation (18) is converted to the following, where T^o is the bulk water temperature and the exit water temperature for the current time step:

$$\frac{T^{o+1} - T^o}{\Delta t} = \frac{\dot{m}}{m}(T_{in} - T^o) \tag{20}$$

which is rearranged to be

$$T^{o+1} = T^o + \Delta t\,\frac{\dot{m}}{m}(T_{in} - T^o) \tag{21}$$

4.2 Effect of HTF Flow Rate

Three experiments were performed with an HTF inlet temperature of approximately 32 °C at flow rates of 1.01, 1.53, and 2.00 L/min. Each experiment began with the PCM, copper tubes, and TES water near room temperature (21-23 °C). The HTF inlet and outlet temperatures were measured by T-type thermocouples before the TES inlet and after the TES outlet, respectively. Due to the differing flow rates produced by the two gear pumps, the gear pump prior to the TES inlet required minor adjustments throughout each experiment to ensure equal flow into and out of the TES unit. The volumetric flow rate was measured during the experiment by a flow meter, and the average flow rate from each experiment was recorded. The adjustments to the gear pump were minor, brief, and infrequent. The results from these three experiments and their corresponding numerical predictions are shown in Figure 4.1. From top to bottom in the figure, the heat transfer coefficients used in the numerical model were 219, 268, and 306 W/m^2-K, respectively.

Before making observations from the results shown in Figure 4.1, two comments must be made. Firstly, the constant temperature of the outlet water at the beginning of the numerical results, seen in Figure 4.1, exists due to the ramifications of the assumptions in the HTF model. With each time step, water is effectively displaced from one control volume to the next. With the entire system at a uniform initial temperature, there is a set length of time before the incoming warm water exits the numerical tube bank and then the TES unit. This length of time is determined by the number of tube columns multiplied by the time step. The time step is determined based upon the amount of time required for water to fill a tube column control volume. With higher flow rates, the time step decreases, lessening this initial time of constant outlet temperature.

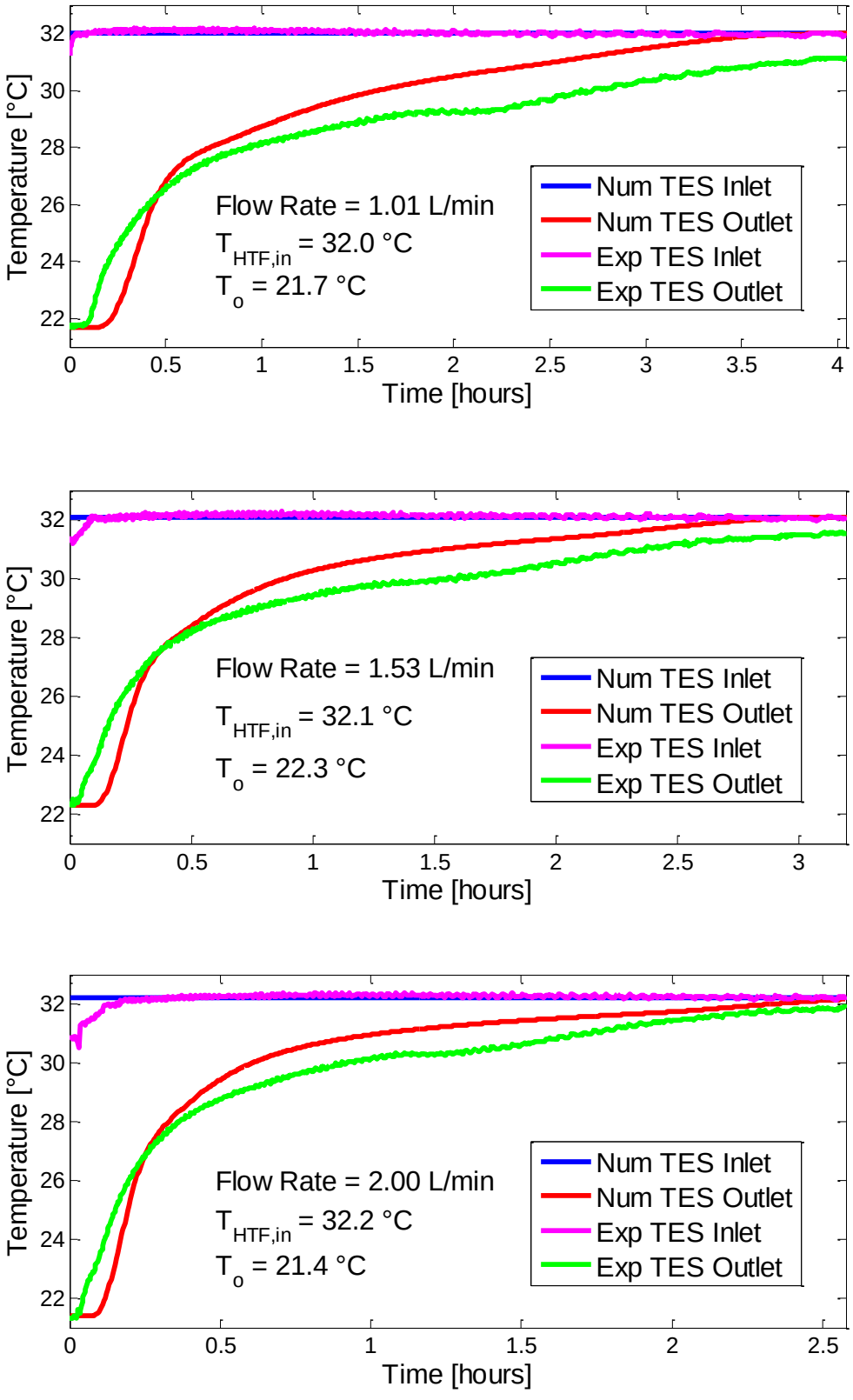

Figure 4.1: HTF Outlet Temperature Profiles at Varying Flow Rates

Secondly, it can be seen in the results in Figure 4.1 that the experimental inlet water temperature drops initially before returning to its set temperature. This issue is more significant in the experiments with high flow rates and also those with high inlet water temperature, as can be seen in the next section. This initial drop in inlet water temperature exists due to the controller in the thermostatic bath. At the beginning of an experiment, water between 21-23 °C enters the thermostatic bath, which is maintaining water at a temperature ten or so degrees higher than what is incoming. This influx of cold water to the thermostatic bath immediately lowers the temperature of the water within the bath, thereby lowering the exit water from the bath. With higher flow rates and higher desired water temperatures, the thermostatic bath is required to expend greater energy to heat the water back to the desired temperature. The thin-film heaters are helpful in providing initial heating before water enters the thermostatic bath, and this prevents the issue from being more significant.

The results in Figure 4.1 show improved accuracy with increasing flow rate. The initial discrepancy in the numerical and experimental outlet temperature profiles is primarily due to the fluid displacement assumption in the numerical model, but as the HTF flow rate increases, the fluid displacement assumption becomes more realistic. The fluid displacement assumption is likely also to be the most significant reason for the long-term difference in the results because it is assumed that the incoming hot water simply displaces the cold resident water in front of it. Numerically, this quickly eliminates the cold water from the tube bank, which is an unrealistic ramification of the displacement assumption. Several experimental factors also exist that help explain the discrepancy

between the numerical and experimental outlet temperature profiles. The following factors apply to all experimental results in this chapter, not only to those in this section.

Firstly, the water within the TES unit is known to have been thermally stratified based upon thermocouple readings of the water around the baffles. Throughout an experiment, the difference in temperature between the water at the top of the unit and the water at the bottom of the unit is between 0-3 °C at the inlet baffle and between 1-5 °C at the outlet baffle. The temperature difference between the inlet and outlet baffles is likely due to the natural convection effects within the water as it cools down while moving through the tube bank. This stratification affected the rate at which the PCM melted within the tubes as well. The uppermost row of tubes tended to melt faster than the bottom row. Additionally, because the bottom two outlet ports from the TES unit were at higher pressure, more water likely exited the unit through the bottom ports, meaning that lower temperature water would have exited the tank for temperature measurement.

Secondly, the phase change material is known to have a melting temperature range of 27-29 °C, while the numerical model uses a single temperature value during phase change. This difference likely contributed in small part to the discrepancy in the numerical and experimental results by bringing down the experimental outlet water temperature initially.

Thirdly, the thermal mixing of the large volumes of water was not perfect, evidenced by the existence of stratification. While this assumption was necessary, it did contribute to the differences between the numerical and experimental results.

Lastly, heat loss from the TES unit to the atmosphere was a concern. To test the effects of heat loss from the unit, an experiment with insulation (R-value of 13 m^2-K/W)

surrounding the unit's sides and lid was performed for comparison. Tube-shaped insulation was also added around the plastic tubing. The results of the two experiments are provided in Figure 4.2, and they show great agreement. The difference between the two initial temperatures of the system is insignificant, being that the sensible heat gained by a 1.12 °C temperature rise in the PCM constitutes less than one percent of the energy gained by latent heat alone. From Figure 4.2 it can be reasonably stated that heat transfer to the atmosphere plays a minimal role in the difference between the numerical and experimental results. The average percent difference between the two runs was 0.9%.

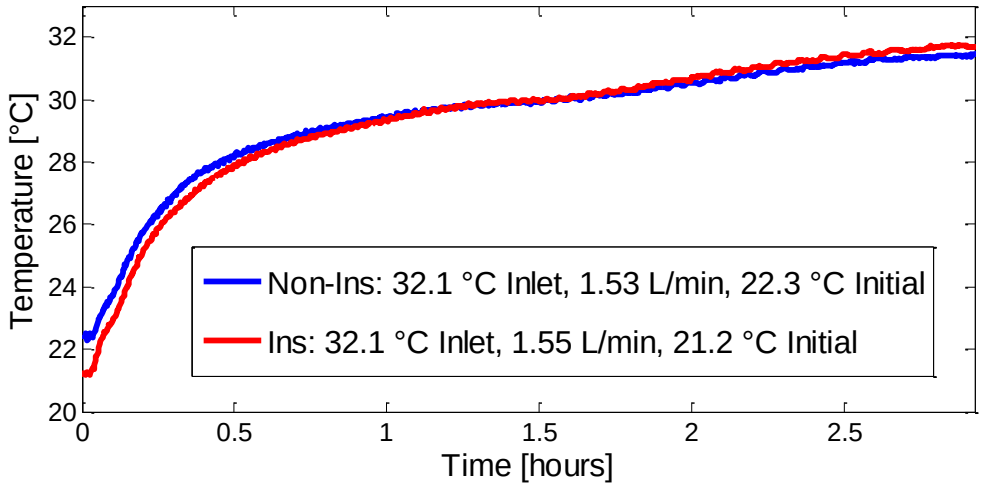

Figure 4.2: Non-Insulated and Insulated Results for Outlet HTF Temperature

The HTF outlet temperature profiles for the three experiments of varying flow rates are shown in Figure 4.3. At higher flow rates, the HTF exited the TES unit at a higher temperature, as expected. Although a higher flow rate produces a higher average heat transfer coefficient, which improves heat transfer, the HTF has less time to interact with the PCM-filled tubes, thereby causing the water to exit at a higher temperature.

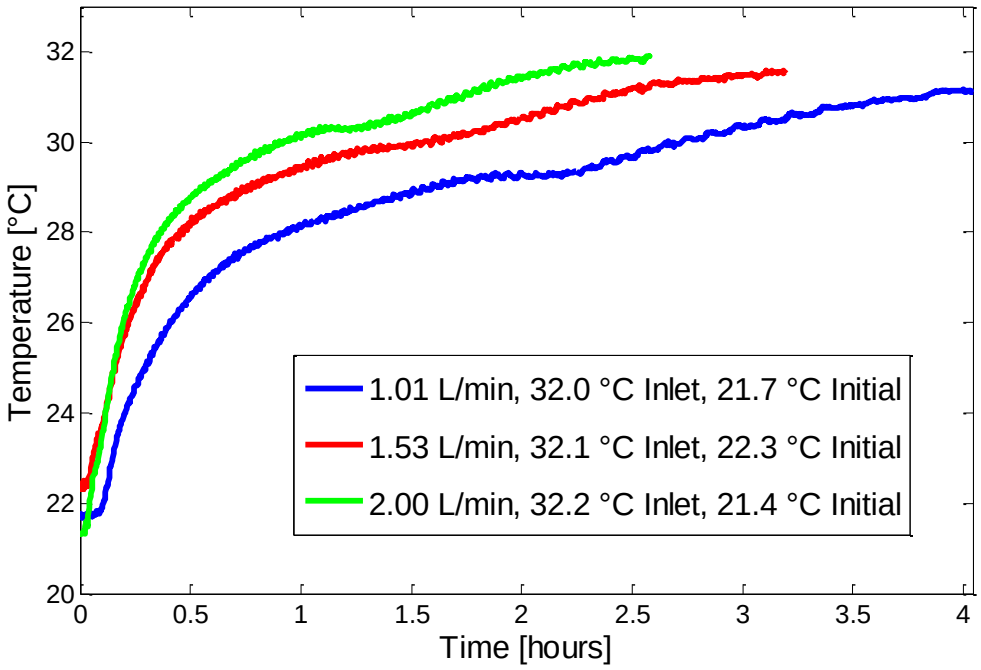

Figure 4.3: Experimental Outlet Temperature Profiles at Varying Flow Rates

It should be noted that while all of the results shown herein are for PCM melting within the TES unit, results for freezing can be reasonably predicted by the melting findings. When considering cases for melting and freezing, a similar HTF outlet temperature profile exists if the following values are the same: the difference between the PCM melting temperature and the system's initial temperature, the difference between the PCM melting temperature and the HTF inlet temperature, and the flow rate. As shown in Figure 4.4, the HTF outlet temperature during PCM freezing is a reflection of the HTF outlet temperature during PCM melting, and this reflection is about the PCM melting/freezing temperature. For perfect reflection it is necessary that the PCM have the same values for the properties in the solid and liquid phases. This is the case for the PCM used for the present study, using a single numerical value for density.

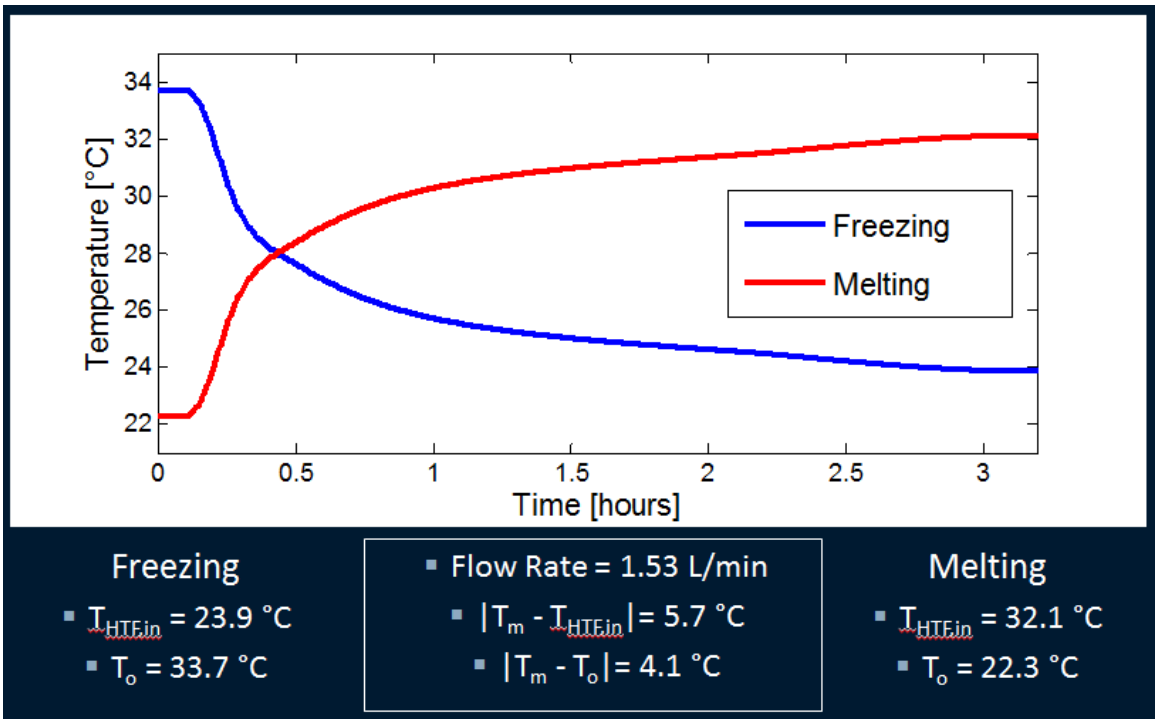

Figure 4.4: Comparing Melting and Freezing Trends

4.3 Effect of HTF Inlet Temperature

To determine the influence of the HTF inlet temperature on the outlet temperature, experiments were performed and compared to the numerical findings. The results are shown in Figure 4.5. From top to bottom in the figure, the heat transfer coefficients used for the numerical simulations were 268, 269, and 269 W/m^2-K, respectively. As discussed previously, there is greater discrepancy between the numerical and experimental results with higher HTF inlet temperatures. This, again, is primarily due to the fluid displacement assumption. The effect of HTF inlet temperature on the charging rate of the TES unit is significant. By raising the inlet water temperature from 32.1 °C to 36.0 °C, the TES unit was charged nearly an hour faster, as seen in Figure 4.6, with the three experimental profiles shown together.

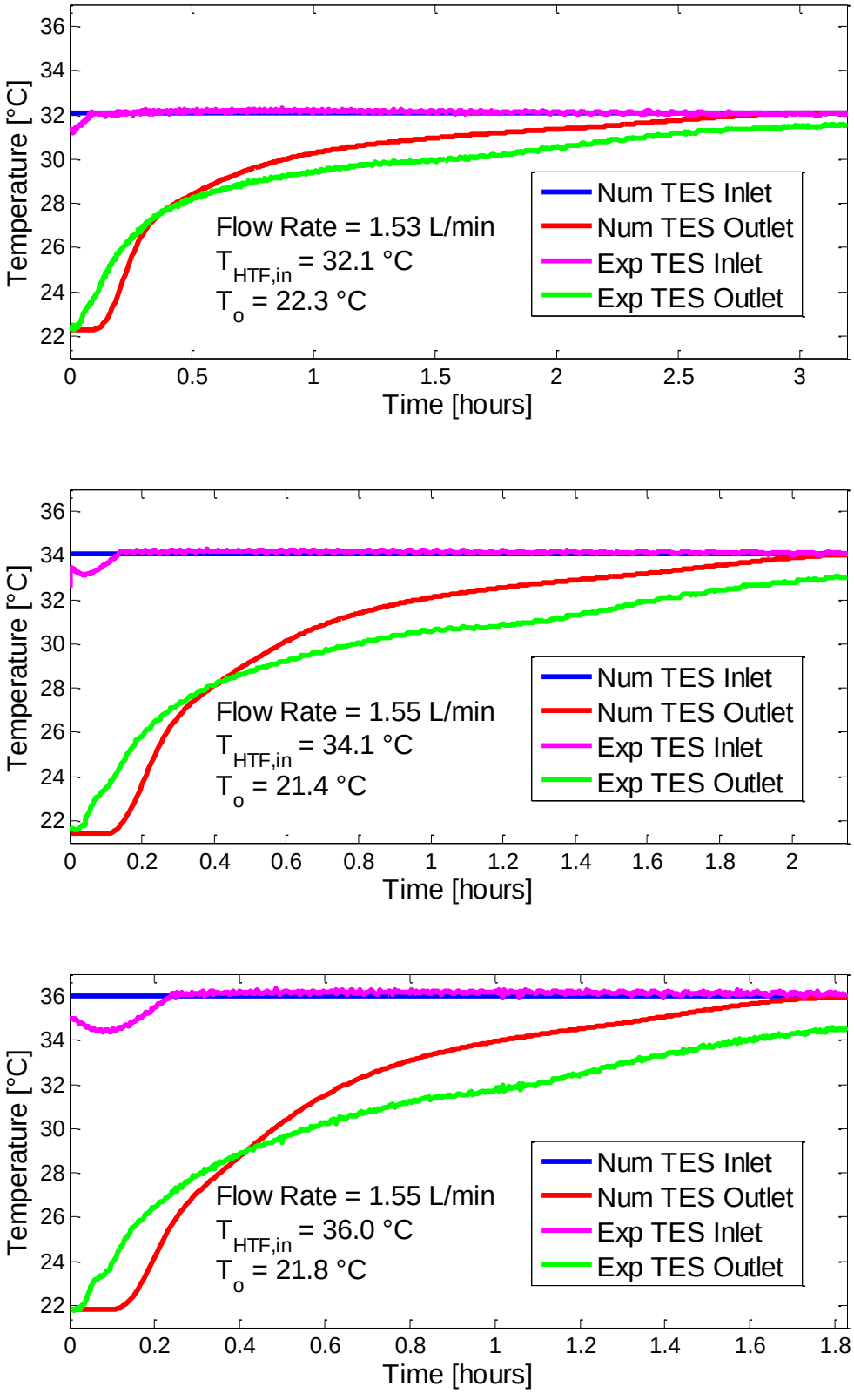

Figure 4.5: HTF Outlet Temperature Profiles at Varying Inlet Temperatures

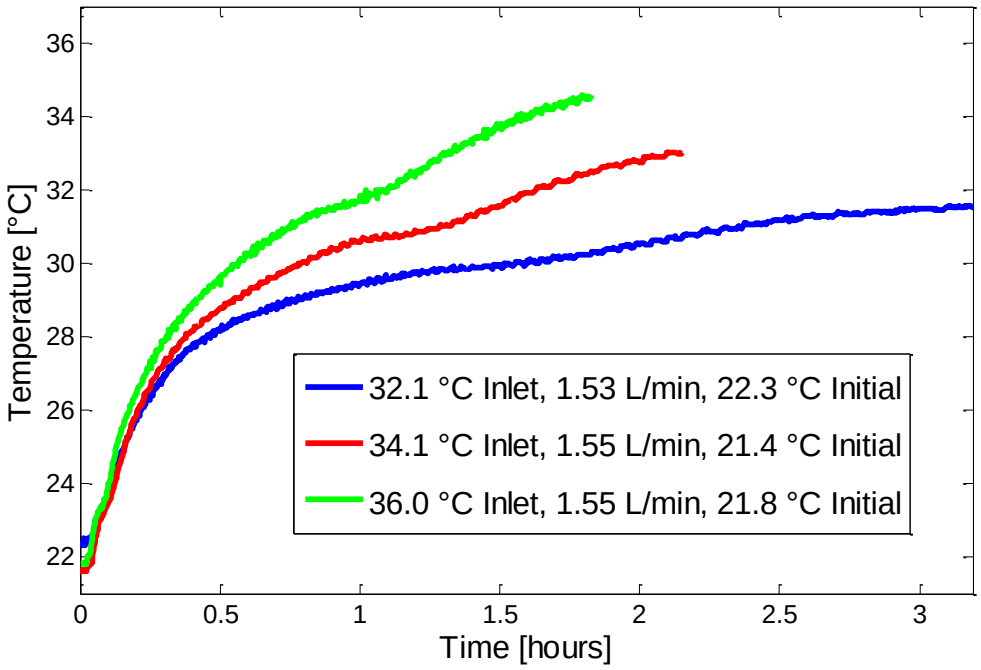

Figure 4.6: Experimental Outlet Temperature Profiles at Varying Inlet Temperatures

4.4 Temperature Profiles of PCM-Filled Tubes

Because the temperatures of both the copper tube and the PCM center were experimentally measured by thermocouples in six tubes, those results can also be used for comparison with the numerical model. While the first few tubes may exhibit different heat transfer characteristics due to differing flow, the tubes later in the tube bank exhibit characteristics more closely aligned with the numerical predictions using the average heat transfer coefficient. The seventh tube from the inlet in the middle row was chosen for comparison between the numerical and experimental results. The numerical and experimental temperature profiles of the copper tube and PCM center are shown for two conditions in Figure 4.7.

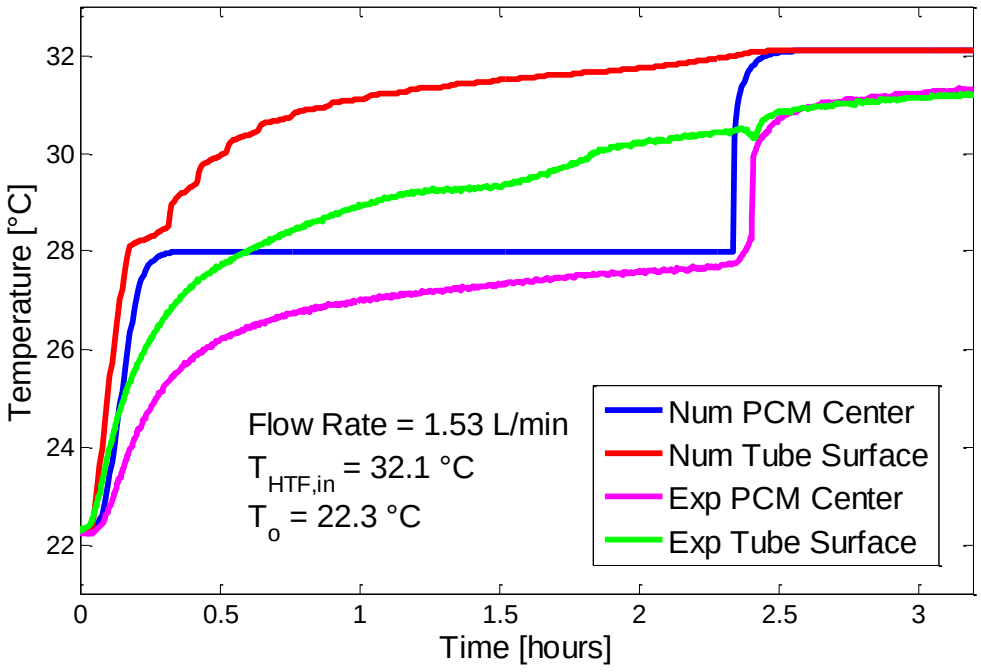

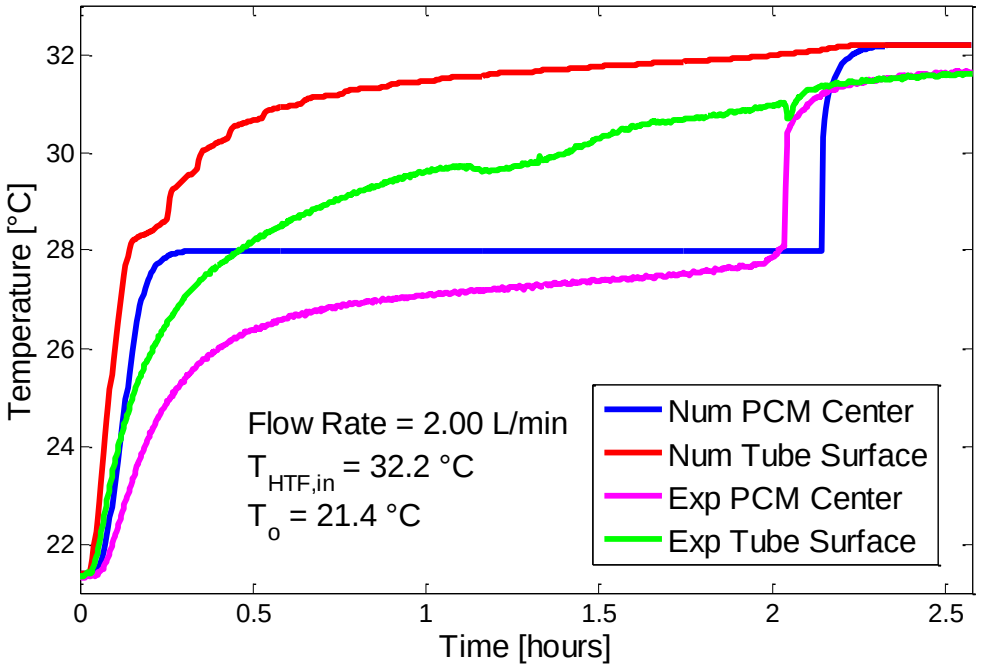

Figure 4.7: Temperature Profiles of Copper Tube and PCM Center

A few observations can be made from Figure 4.7. Firstly, the existence of a melting temperature range is apparent in the experimental results based on the slow rise of the PCM center temperature. Secondly, neither the experimental tube surface temperature nor the experimental PCM center temperature rises to its corresponding numerical temperature. Based upon the results of the HTF outlet temperatures, these temperature profiles would be expected. The same issues that caused the HTF outlet temperatures to be offset cause these temperatures to be offset. Lastly, the experimental PCM center temperature melts at nearly the same time as the numerical prediction, which is important because knowing when the latent heat of the PCM is fully expended is useful in TES applications. The PCM center is considered melted when the sharp rise in temperature occurs near 28 °C.

4.5 Repeatability

To demonstrate repeatability, the experiments with the highest flow rate and the highest HTF inlet temperature performed again. For the setup with the highest HTF flow rate, the average percent difference between the two runs was 0.451%. For the one with the highest HTF inlet temperature, the average percent difference between the two runs was 0.592%. These small differences indicate excellent repeatability. The HTF outlet temperature profiles for these two repeatability tests are provided in Figure 4.8 for comparison.

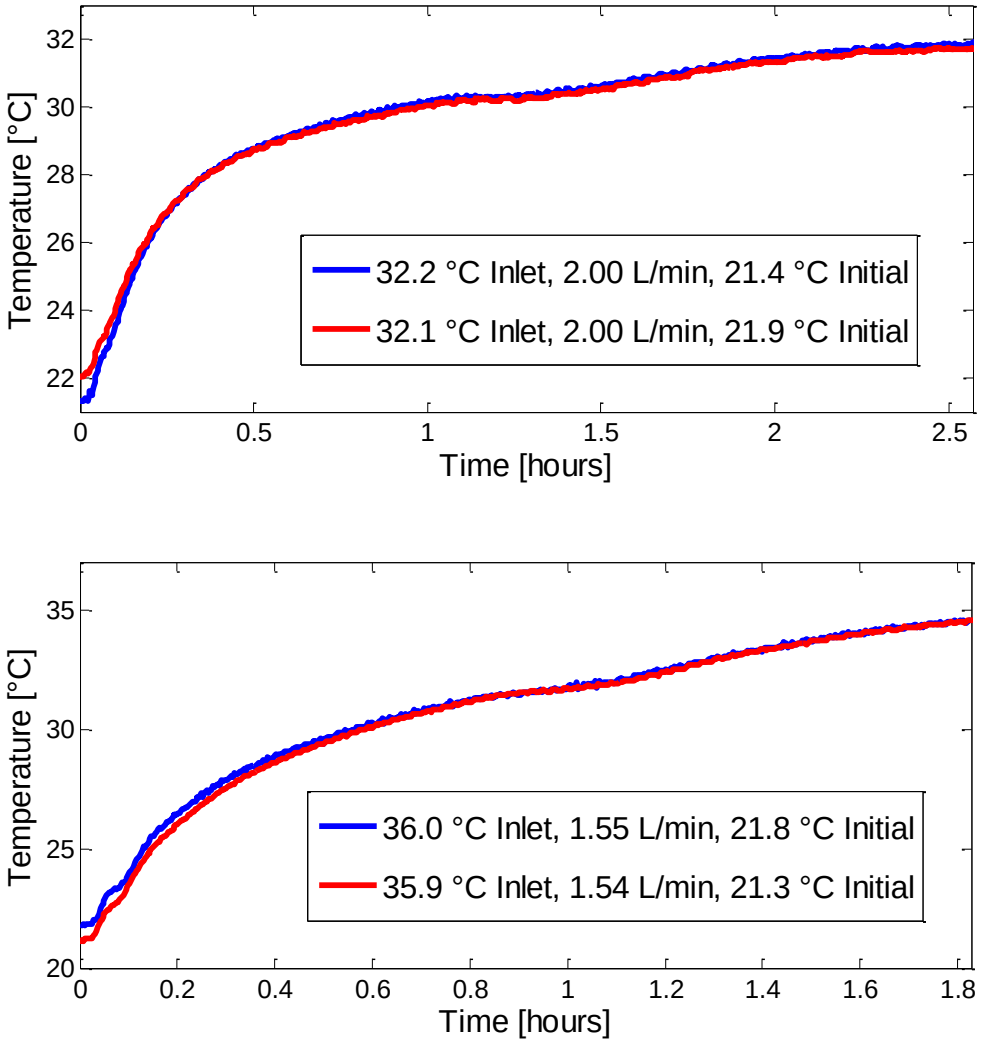

Figure 4.8: Repeatability Tests - HTF Outlet Temperature Profiles

4.6 Numerical Results with Larger Tube Bank

There is one very important characteristic of larger tube banks that cannot be seen in the results shown thus far. To show this attribute of larger tube banks, the numerical model was used to simulate a tube bank of the same dimensions as those shown previously except for the addition of columns to make the tube bank 100 columns long. The average heat transfer coefficient used for this simulation was 265.0 W/m^2-K. Figure

4.9 shows the temperature profiles of the HTF as it passes through every twentieth column of the tube bank. For this simulation the water enters the tube bank immediately, rather than having any volume of fluid before or after the tube bank, as in the experimentation.

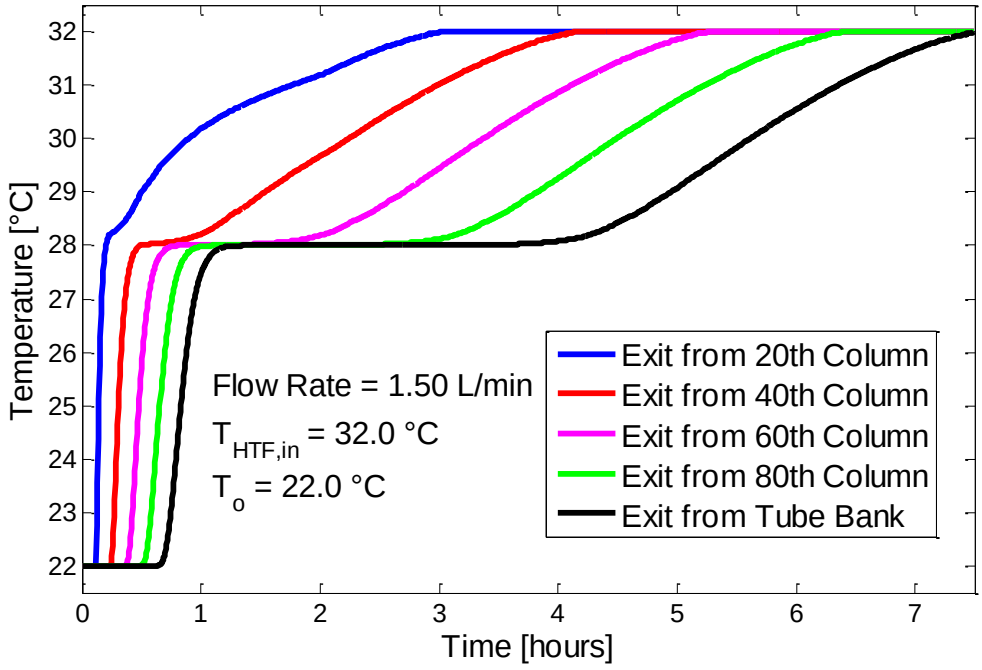

Figure 4.9: HTF Outlet Temperature Profiles for 100 Column Tube Bank

The assumption of fluid displacement by control volumes is more noticeable numerically in this case due to the number of columns of tubes. 100 time steps are required before the inlet HTF reaches the exit from the tube bank. The primary characteristic of these results, however, is the constant temperature at which the HTF exits the tube bank from hour one to nearly hour four. This constant temperature is the PCM's melting temperature. With longer tube banks, a stable HTF outlet temperature is possible. It can be seen in Figure 4.9 that with each additional twenty columns of tubes,

this configuration provides approximately one more hour of stable HTF outlet temperature. This is especially important in applications that require a stable HTF temperature for lengthy periods of time, such as a TES unit for data center use.

4.7 Numerical Results with Higher PCM Thermal Conductivity

Numerical investigation into the effect of PCM thermal conductivity on discharging rates and HTF outlet temperature profiles was also performed. Using the same setup as described in the previous sections (with sixteen columns), three numerical simulations were performed, each with a different PCM thermal conductivity (0.2, 2.0, and 20.0 W/m-K). A higher effective thermal conductivity can be achieved in actual applications with the addition of another material with a high thermal conductivity, such as copper.

Figure 4.10 shows the amount of energy stored in the PCM and copper as a fraction of the total available sensible and latent heat between 22-32 °C. Figure 4.11 shows the HTF outlet temperature profiles of the three numerical simulations. There are differences in the storage times and the temperature profiles of these three cases, indicating that the PCM thermal conductivity does play an important role in the charging and discharging rates. With the PCM at high thermal conductivities (2.0 and 20.0 W/m-K), the profiles look very similar. With the PCM at a lower thermal conductivity (0.2 W/m-K), however, the profiles are noticeably different.

While it is interesting to see the difference in discharging times between the different cases in Figure 4.10, the HTF outlet temperature profiles are of greater interest. It is observed that with higher PCM thermal conductivities, the HTF exits the tube bank at lower temperatures for approximately the first hour. This is due to the increased heat

transfer rate caused by the higher thermal conductivity. After the PCM has melted significantly, the HTF outlet temperature rises quickly, since there is little cold energy remaining in the PCM. From Figure 4.11 it is also observed that with a higher PCM thermal conductivity, it is easier to achieve a nearly constant HTF outlet temperature. This is due to the fact that the PCM is melting significantly faster, as seen in Figure 4.10, which allows the HTF to chill throughout the tube bank more quickly. The shell-and-tube configuration does mitigate some of the negative effects of the low thermal conductivity of the PCM. Unlike many concentric units discussed in the literature, this shell-and-tube design does not require an inordinate amount of time to discharge the unit with a PCM of low thermal conductivity.

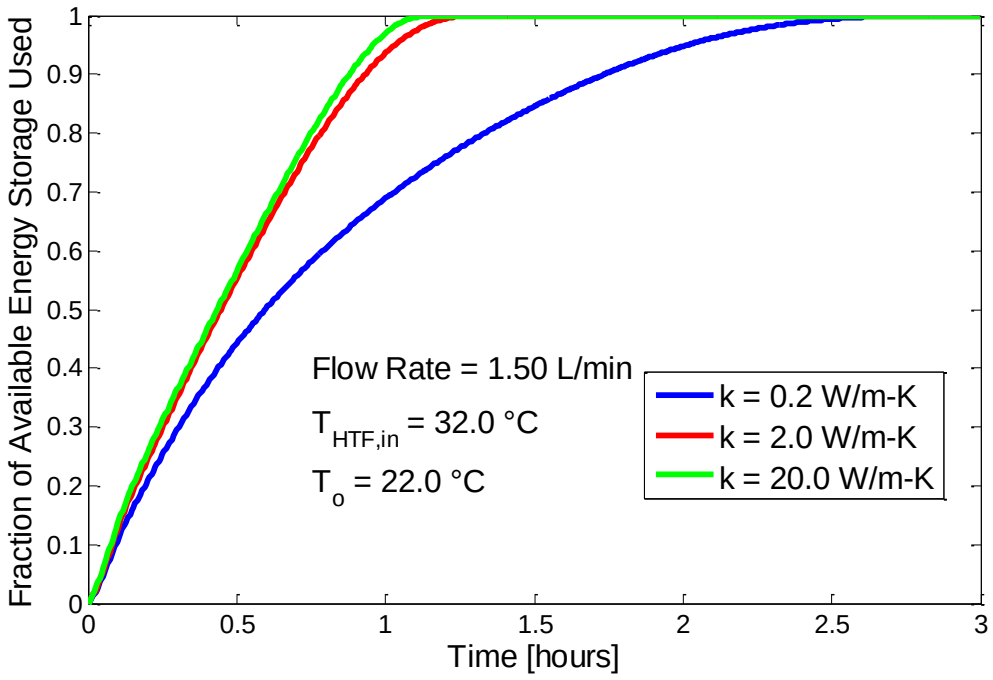

Figure 4.10: Fraction of Used Energy with Varying PCM Thermal Conductivities

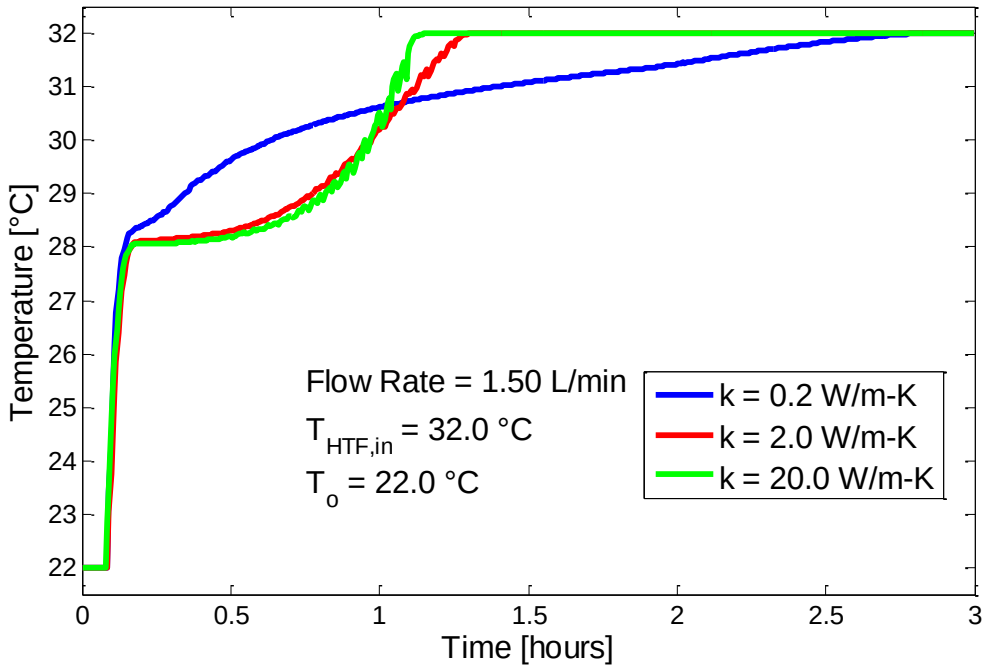

Figure 4.11: HTF Outlet Temperature with Varying PCM Thermal Conductivities

4.8 Two-Dimensional Polar Model within TES Unit

A two-dimensional polar model for the PCM-filled tubes was created, since the heat transfer coefficient is known to vary along the surface of the tube. This two-dimensional model has been evaluated alongside the one-dimensional model, and the two show excellent agreement. A heat transfer coefficient profile is prescribed to the cylindrical surface, as shown in Figure 4.12. This particular profile has been chosen to reflect the trends found by Rao [46]. The exact values for each angular position were chosen such that there would be a significant difference between the maximum and minimum values, imposing a greater potential for discrepancy in the one- and two-dimensional models. The average of all the values is used as the average heat transfer coefficient for the one-dimensional model, and for the case shown, this value is 265 W/m^{2}K. Figure 4.13 shows

the results of the two models using the standard sixteen column tube bank discussed throughout this section. With a thick copper tubing, the effect of the local heat transfer coefficients could be somewhat mitigated by the highly conductive copper; therefore, the copper is chosen to be infinitesimal to allow maximum discrepancy in the results.

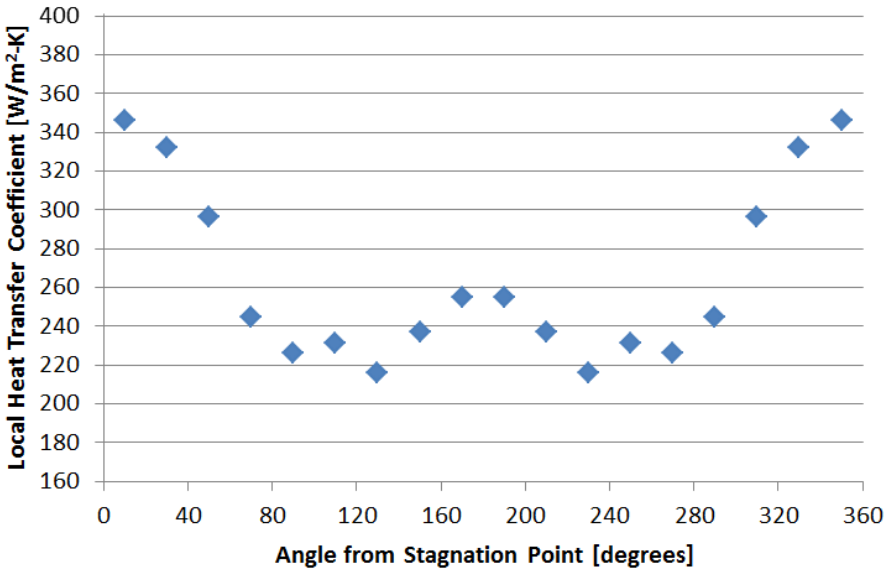

Figure 4.12: Heat Transfer Coefficient Profile along Cylindrical Surface

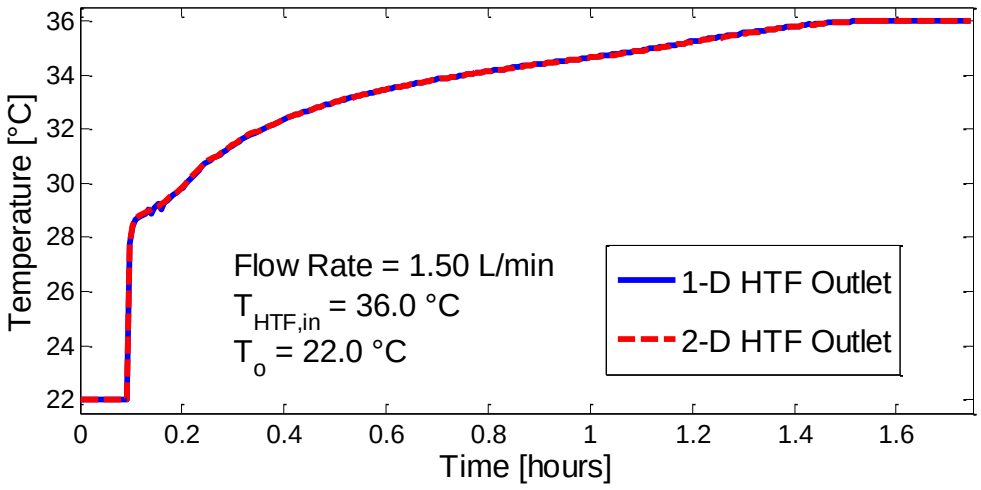

Figure 4.13: Comparison of One- and Two-Dimensional Models

The profiles seen in Figure 4.13 are very similar, and this is due in part to the miniscule difference the heat transfer coefficient has on the melting time between the values of 346 and 216 W/m^{2}K, the highest and lowest heat transfer coefficient values in the two-dimensional model. Figure 4.14 shows the effect of the heat transfer coefficient on the HTF outlet temperature with the one-dimensional model. From these results, it can be concluded that the one-dimensional model is sufficient for modeling phase change within a cylinder with the assumption of conduction-dominated heat transfer. If, however, convection was known to be significant, a two-dimensional model would be of greater benefit.

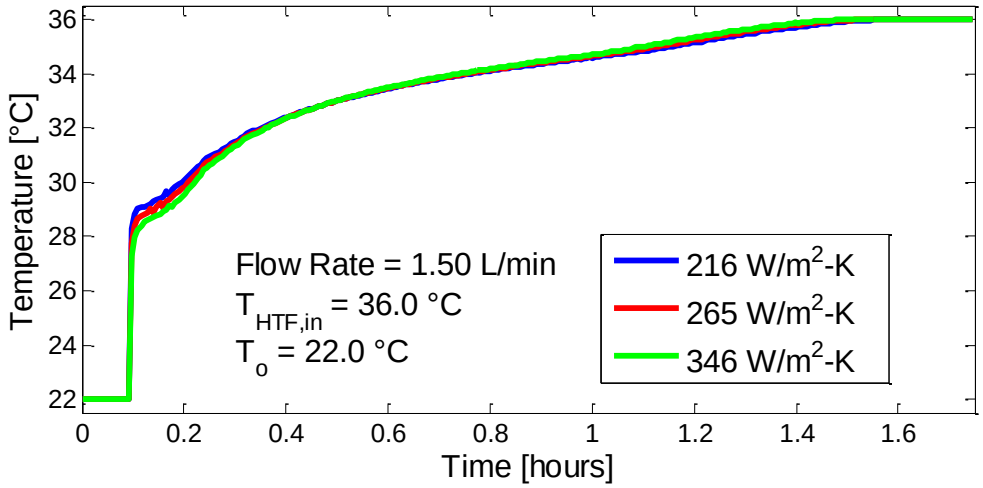

Figure 4.14: Effect of Heat Transfer Coefficient on the HTF Outlet Temperature

4.9 Application of TES Unit to Server Cooling

The application of a TES unit into a data center requires an understanding of the cooling requirement and the amount of space available for the unit. As shown previously, lengthy TES units allow the HTF to maintain a stable outlet temperature for long periods of time. By increasing the width and height of the unit, the HTF outlet temperature can be

maintained for even longer. The cooling requirement and the special constraints within the data center will determine the size of the unit and the number of PCM-filled tubes. Table 4.1 shows the amount of cooling time provided by the TES unit to a specified heat load. The heat loads were chosen to represent the necessary heat dissipation from one to five racks, dissipating 20 kW of heat each.

Table 4.1: Data Center Application Results

Load (kW)	Flow (L/min)	Length (m)	Width (m)	Height (m)	# Tubes	Time (hrs)
20	47.86	1.52 (4.99 ft)	1.829 (6 ft)	1.829 (6 ft)	3876	5.9
25	59.83	3.04 (9.98 ft)	1.829 (6 ft)	1.219 (4 ft)	5187	6.2
25	59.83	3.04 (9.98 ft)	0.914 (3 ft)	2.438 (8 ft)	10374	7.2
30	71.79	3.04 (9.98 ft)	1.219 (4 ft)	1.829 (6 ft)	7752	5.5
50	119.65	3.04 (9.98 ft)	1.829 (6 ft)	2.438 (8 ft)	10374	6.3
60	143.58	6.11 (20.04 ft)	1.219 (4 ft)	1.829 (6 ft)	15572	5.6
80	191.44	6.11 (20.04 ft)	1.829 (6 ft)	1.829 (6 ft)	15572	6.0
100	239.30	6.11 (20.04 ft)	1.829 (6 ft)	2.438 (8 ft)	20839	6.4

For the results shown in Table 4.1, the TES unit begins in a charged state at 22 °C. Water enters the TES unit at a constant temperature of 34 °C, and the water's outlet temperature is maintained by the unit at or below the PCM's melting temperature of 28 °C. When the water begins to exit the unit at 28.2 °C, the TES unit is considered to be discharged to the point at which it is no longer able to meet the cooling requirement, based upon the conservation of energy between the heat load, the PCM-filled tubes, and the water. The tubes' diameters, properties, and transverse and longitudinal pitches are the same as those used to obtain all previous results, and these values can be found in Table 3.2 and Table 3.3.

4.10 PCM Leakage

Throughout the course of experimentation, it was noticed that PCM slowly leaked from some of the instrumented tubes. The PCM leaked due to the inability to perfectly seal around the thermocouple wires exiting the rubber stoppers at the end of the tubes. Because the thermocouple wires have two small insulated wires of copper and constantan held together, a very small groove exists on either side of their joined region. To explain further, the two insulated wires are circular in cross-section, and being joined together side-by-side, they do not connect flush with one another because of their circular shape. When using the epoxy to seal around the thermocouple wire that exits the rubber stopper, it is not possible to ensure perfect sealing in and around the two grooves that exist on the thermocouple wire. It is between these tiny grooves that the PCM slowly leaked during melting. The PCM, having a lower density than the water, rose to the top of the TES unit, and after the final experiment, the leaked PCM was measured. 108.2 grams of PCM leaked through the course of the eight experiments. This represents 2.33% of the total PCM within the TES unit at the beginning of the first experiment. To demonstrate the effect of this lost PCM on the HTF outlet temperature, Figure 4.15 shows the comparison of the numerically predicted HTF outlet temperatures before and after leakage. The percent difference between the two runs was 0.064%. For the "After Leakage" simulation, the lost PCM was taken equally from the diameter of every tube, and it agrees very well with the "Before Leakage" results. While not every tube lost PCM, this is the best possible representation of the effect of leakage, given the inability to discern how much each experimental tube lost individually.

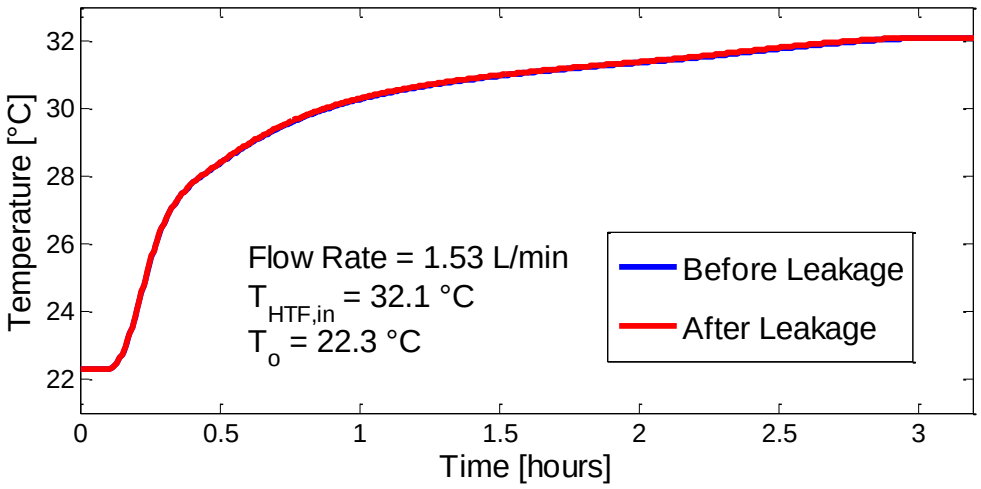

Figure 4.15: HTF Outlet Temperature - Effect of PCM Leakage

4.11 Uncertainty

To determine the uncertainty in the temperature measurements of the T-type thermocouples, the following representative calculations were performed. Calibration was performed by comparing the temperature reading of a dry block calibrator to the temperature measured by the thermocouples inserted into the dry block calibrator and connected to the data acquisition center. Using thirty-six thermocouples from the same company and same batch, it has been assumed that the thermocouples are made from the same materials, and therefore have the same bias and variation. 216 total temperature values were measured during the calibration process.

First, the sample mean temperature was calculated, as seen in Eq. (22).

$$\bar{x} = \frac{\sum x_i}{n} = \frac{(12.23\ °C) + \cdots + (43.98\ °C)}{216} = 27.89\ °C \qquad (22)$$

Next, the squared difference between the sample mean temperature and each sample temperature was added, which provides the means by which the sample standard deviation can be calculated, as in Eq. (24).

$$\sum(x_i - \bar{x})^2 = \sum((12.23\ °C) - (27.89\ °C))^2 + \cdots = 26758\ °C^2 \quad (23)$$

$$S_x = \sqrt{\frac{(\sum(x_i - \bar{x})^2)}{n-1}} = \sqrt{\frac{(26758\ °C^2)}{216-1}} = 11.16\ °C \quad (24)$$

The standard deviation is then used to calculate the Type A uncertainty.

$$U_A = \frac{S_x}{\sqrt{n}} = 0.76\ °C \quad (25)$$

The first Type B uncertainty is based upon the uncertainty in the calibration of the dry block calibrator, a value provided by the company. The second Type B uncertainty is based upon the resolution of the dry block calibrator, and this is calculated by dividing by half the resolution of the calibrating component, which in this case was 0.1 °C.

$$U_{B1} = U_{Cal} = 0.031\ °C \quad (26)$$

$$U_{B2} = U_{Res} = 0.05\ °C \quad (27)$$

The combined uncertainty is then calculated as seen in Eq. (28).

$$U_C = \sqrt{U_A^2 + U_{B1}^2 + U_{B2}^2} = 0.76\,°C \tag{28}$$

Finally, the expanded uncertainty, based upon a 95% confidence level and a student's t k-factor of 1.652, is calculated.

$$U_{95} = U_C \times k_f = 0.76\,°C \times 1.652 = 1.26\,°C \tag{29}$$

The uncertainty in the flow rate, based upon the manufacturer's specifications for the flow meter, is 1.0%, and the uncertainty in the total PCM mass is 0.12%.

CHAPTER 5

CONCLUSION

As the cooling requirement in data centers continues to rise, cost-effective solutions for providing this cooling are becoming increasingly valued. Because electricity often costs more during peak hours of electrical usage, it is incumbent upon companies to find ways to avoid spending unnecessarily during these peak hours. By shifting a measure of electrical usage to off-peak hours, data centers can save on electricity costs. Since chilled water is used in some capacity for most electronic cooling applications in data centers, a TES unit, which stores cold energy, can be employed. This TES unit can be charged during off-peak hours by freezing the PCM, and then discharged during peak hours, cooling water and saving on electrical costs.

In the pursuit to develop a model to characterize the HTF outlet temperature from a shell-and-tube TES unit, two primary numerical components were coupled together. A fully-implicit transient one-dimensional control volume formulation that employs the enthalpy method for phase change was developed first to determine the transient local gain or loss of energy within a PCM-filled tube. This formulation was then combined with a global energy balance to determine the bulk HTF temperature within each column of the tube bank, ultimately providing the exit HTF temperature from the TES unit. The numerical results were compared with experimental results to determine the reliability of the numerical model. The investigated TES unit, having 0.316 kWh of latent heat, was charged more than one hour faster with an increase from 1.01 L/min to 2.00 L/min in the

inlet water flow rate. By increasing the inlet water temperature from 32.1 °C to 36.0 °C, the unit was also charged more than one hour faster.

With the numerical and experimental results showing similar trends but not full agreement, several reasons exist to explain their discrepancies. It was noted that with increasing flow rates, the numerical model tends to agree more closely with the experimental results. The effect of the HTF volumetric flow rate and inlet temperature are shown to impact the HTF outlet temperature profile and the TES unit's charging and discharging rates. Numerical results also showed two important storage characteristics. Firstly, they showed that with a sufficiently long tube bank, a constant HTF outlet temperature is obtainable. Secondly, it was shown that increasing the effective thermal conductivity of the PCM effectively increased the charging and discharging rates. With improvements to the HTF model, the PCM-HTF coupled numerical model could be a valuable resource for real-time use within data centers.

REFERENCES

[1] Mitchell-Jackson, J., Koomey, J.G., Blazek, M., Nordman, B., 2002, "National and regional implications of internet data center growth in the US", Resources, Conservation & Recycling, 36, pp. 175-185.

[2] Koomey, J., 2011, "Growth in data center electricity use 2005 to 2010", Oakland, CA: Analytics Press, July, www.analyticspress.com/datacenters.html. Accessed April 2015.

[3] Zhang, H., Shao, S., Xu, H., Zou, H., Tian, C., 2014, "Free cooling of data centers: A review", Renewable and Sustainable Energy Reviews, 36, pp. 171-182.

[4] Iyengar, M., Schmidt, R.R., 2007, "Analytical Modeling of Energy Consumption and Thermal Performance of Data Center Cooling Systems – from the Chip to the Environment", Proceedings of the ASME InterPACK Conference 2007, 1, pp. 877-886.

[5] Ebrahimi, K., Jones, G.F., Fleischer, A.S., 2014, "A review of data center cooling technology, operating conditions and the corresponding low-grade waste heat recovery opportunities", Renewable and Sustainable Energy Reviews, 31, pp. 622-638.

[6] "TIA-942: Standardization For Data Centers", Technology Enthusiast, www.WordPress.com; 2012. Accessed April 2015.

[7] Greenberg, S., Mills, E., Tschudi, B., 2006, "Best Practices for Data Centers: Lessons Learned from Benchmarking 22 Data Centers", Proceedings of 14th ACEEE Summer Study on Energy Efficiency in Buildings, Pacific Grove, CA.

[8] Coles, H., Greenberg, S., 2014, "Direct Liquid Cooling for Electronic Equipment", Ernest Orlando Lawrence Berkeley National Laboratory, LBNL-6641E.

[9] Rutberg, M., Cooperman, A., Bouza, A., 2013, "Data Center Cooling", American Society of Heating Refrigeration and Air-Conditioning Engineers Journal, 55 (10), pp. 82, 84-86.

[10] Pielichowska, K., Pielichowski, K., 2014, "Phase change materials for thermal energy storage", Progress in Materials Science, 65, pp. 67-123.

[11] Sharma, A., Tyagi, V.V., Chen, C.R., Buddhi, D., 2009, "Review on thermal energy storage with phase change materials and applications", Renewable & Sustainable Energy Reviews, 13 (2), pp. 318-345.

[12] Lingayat, A.B., Suple, Y.R., 2013, "Review On Phase Change Material As Thermal Energy Storage Medium: Materials, Application", International Journal of Engineering Research and Applications, 3 (4), pp. 916-921.

[13] Chiu, J., Martin, V., Setterwall, F., 2009, "A Review of Thermal Energy Storage Systems with Salt Hydrate Phase Change Materials for Comfort Cooling", 11th International Conference on Thermal Energy Storage, June 14-17, Stockholm, Sweden.

[14] Oró, E., de Gracia, A., Castell, A., Farid, M.M., Cabeza, L.F., 2012, "Review on phase change materials (PCMs) for cold thermal energy storage applications", Applied Energy, 99, pp. 513-533.

[15] Bledjian, L., Hale, D.V., Hoover, M.J., O'Neill, M.J., 2002, "Chapter 11 – Phase-Change Materials", Spacecraft Thermal Control Handbook, Volume I: Fundamentals Technologies (2nd Edition), pp. 373-403.

[16] Mondal, S., 2008, "Phase change materials for smart textiles – An overview", Applied Thermal Engineering, 28, pp. 1536-1550.

[17] Outlast - Where to use Outlast® technology, www.outlast.com; 2014. Accessed April 2015.

[18] Chidambaram, L.A., Ramana, A.S., Kamaraj, G., Velraj, R., 2011, "Review of solar cooling methods and thermal storage options", Renewable & Sustainable Energy Reviews, 15, pp. 3220-3228.

[19] Kalnæs, S.E., Jelle, B. P., 2015, "Phase change materials and products for building applications: A state-of-the-art review and future research opportunities", Energy and Buildings, 94, pp. 150-176.

[20] Agyenim, F., Hewitt, N., Eames, P., Smyth, M., 2010, "A Review of Materials, Heat Transfer and Phase Change Problem Formulation for Latent Heat Thermal Energy Storage Systems (LHTESS)", Renewable and Sustainable Energy Reviews, 14, pp. 615-628.

[21] Parry, A.J., Eames, P.C., Agyenim, F.B., 2014, "Modeling of Thermal Energy Storage Shell-and-Tube Heat Exchanger", Heat Transfer Engineering, 35 (1), pp. 1-14.

[22] Office of Energy Efficiency & Renewable Energy – Innovative Thermal Energy Storage for Baseload Solar Power Generation, www1.eere.energy.gov; 2014. Accessed April 2015.

[23] Trp, A., 2005, "An experimental and numerical investigation of heat transfer during technical grade paraffin melting and solidification in a shell-and-tube latent thermal energy storage unit", Solar Energy, 79 (6), pp. 648–660.

[24] Trp, A., Lenic, K., Frankovic, B., 2006, “Analysis of the influence of operating conditions and geometric parameters on heat transfer in water–paraffin shell-and-tube latent thermal energy storage unit”, Applied Thermal Engineering, 26 (16), pp. 1830–1839.

[25] Vyshak, N.R., Jilani, G., 2007, “Numerical analysis of latent heat thermal energy storage system”, Energy Conversion & Management, 48 (7), pp. 2161–2168.

[26] Agyenim, F., Eames, P., Smyth, M., 2009, “A comparison of heat transfer enhancement in a medium temperature thermal energy storage heat exchanger using fins”, Solar Energy, 83 (9), pp. 1509–1520.

[27] Agyenim, F., Eames, P., Smyth, M., 2010, “Heat transfer enhancement in medium temperature thermal energy storage system using a multitube heat transfer array”, Renewable Energy, 35 (1), pp. 198–207.

[28] Agyenim, F., Hewitt, N., 2010, “The development of a finned phase change material (PCM) storage system to take advantage of off-peak electricity tariff for improvement in cost of heat pump operation”, Energy and Buildings, 42 (9), pp. 1552–1560.

[29] Agyenim, F., Eames, P., Smyth, M., 2011, “Experimental study on the melting and solidification behaviour of a medium temperature phase change storage material (Erythritol) system augmented with fins to power a LiBr/H2O absorption cooling system”, Renewable Energy, 36 (1), pp. 108–117.

[30] Mosaffa, A.H., Talati, F., Tabrizib, H.B., Rosen, M.A., 2012, “Analytical modeling of PCM solidification in a shell and tube finned thermal storage for air conditioning systems”, Energy and Buildings 49, pp. 356–361.

[31] Ezan, M.A., Ozdogan, M., Erek, A., 2011, “Experimental study on charging and discharging periods of water in a latent heat storage unit”, International Journal of Thermal Sciences, 50 (11), pp. 2205–2219.

[32] Dubovsky, V., Ziskind, G., Letan, R., 2011, “Analytical model of a PCM-air heat exchanger”, Applied Thermal Engineering, 31 (16), pp. 3453-3462.

[33] Hosseini, M.J., Ranjbar, A.A., Sedighi, K., Rahimi, M., 2012, “A combined experimental and computational study on the melting behavior of a medium temperature phase change storage material inside shell and tube heat exchanger”, International Communications in Heat and Mass Transfer 39 (9), pp. 1416–1424.

[34] Hosseini, M.J., Rahimi, M., Bahrampouri, R., 2014, “Experimental and computational evolution of a shell and tube heat exchanger as a PCM thermal storage system”, International Communications in Heat and Mass Transfer, 50, pp. 128–136.

[35] Kibria, M.A., Anisur, M.R., Mahfuz, M.H., Saidur, R., Metselaar, I.S.H.C., 2014, "Numerical and experimental investigation of heat transfer in a shell and tube thermal energy storage system," International Communications in Heat and Mass Transfer, 53, pp. 71-78.

[36] Patankar, S.V., 1980, Numerical Heat Transfer and Fluid Flow. Hemisphere Publishing Corporation, Washington, DC, pp. 41-77, Chap. 4.

[37] Voller, V.R., 1990, "Fast Implicit Finite-Difference Method for the Analysis of Phase Change Problems", Numerical Heat Transfer, Part B, 17, pp. 155-169.

[38] Costa, M., Buddhi, D., Oliva, A., 1998, "Numerical Simulation of a Latent Heat Thermal Energy Storage System with Enhanced Heat Conduction", Energy Conversion & Management, 39 (3-4), pp. 319-330.

[39] Voller, V.R., Cross, M., 1981, "Estimating the Solidification/Melting Times of Cylindrically Symmetric Regions", International Journal of Heat and Mass Transfer, 24 (9), pp. 1457-1462.

[40] Teggar, M., Mezaache, E., Benchatti, A., Zeghmati, B., 2010, "Comparative Study of Heat Transfer during Solidification of Phase Change Materials inside Three Different Capsules", International Journal of Heat and Technology, 28 (2), pp. 19-24.

[41] Chung, J.D., Lee, J.S., Yoo, H., 1997, "Thermal instability during the melting process in an isothermally heated horizontal cylinder", International Journal of Heat and Mass Transfer, 40 (16), pp. 3899-3907.

[42] RubiTherm GmbH. RT – data sheets, www.rubitherm.com; 2013. Accessed April 2015.

[43] Rouault, F., Bruneau, D., Sebastian, P., Lopez, J., 2013, "Numerical modelling of tube bundle thermal energy storage for free-cooling of buildings", Applied Energy, 111, pp. 1099-1106.

[44] Assis, E., Katsman, L., Ziskind, G., Letan, R., 2007, "Numerical and experimental study of melting in a spherical shell", International Journal of Heat and Mass Transfer, 50, pp. 1790-1804.

[45] Zukauskas, A., "Heat Transfer from Tubes in Cross Flow" in J. P. Hartnett and T. F. Irvine, Jr., Eds., Advances in Heat Transfer, Vol. 8, Academic Press, New York, 1972.

[46] Rao, B.K., 2000, "Heat transfer to non-Newtonian flows over a cylinder in cross flow", International Journal of Heat and Fluid Flow, 21 (6), pp. 693-700.